Hydrogen embrittlement in Al-Zn-Mg alloys: Semispontaneous decohesion of precipitates

Shimizu, Kazuyuki
Faculty of Engineering, Tottori University

Toda, Hiroyuki
Department of Mechanical Engineering, Kyushu University

Hirayama, Kyosuke
Department of Engineering and Design, Kagawa University

Fujihara, Hiro
Department of Mechanical Engineering, Kyushu University

他

出版情報：International Journal of Hydrogen Energy. 109, pp.1421-1436, 2025-03-14. Elsevier
バージョン：

International Journal of Hydrogen Energy 109 (2025) 1421–1436

Contents lists available at ScienceDirect

International Journal of Hydrogen Energy

journal homepage: www.elsevier.com/locate/he

Hydrogen embrittlement in Al–Zn–Mg alloys: Semispontaneous decohesion of precipitates

Kazuyuki Shimizu [a,*], Hiroyuki Toda [b,**], Kyosuke Hirayama [c], Hiro Fujihara [b], Tomohito Tsuru [d], Masatake Yamaguchi [e], Taisuke T. Sasaki [f], Masayuki Uesugi [g], Akihisa Takeuchi [g]

[a] Faculty of Engineering, Tottori University, Tottori, 680-8552, Japan
[b] Department of Mechanical Engineering, Kyushu University, Fukuoka, 819-0395, Japan
[c] Department of Engineering and Design, Kagawa University, Kagawa, 760-0016, Japan
[d] Nuclear Science Research Center, Japan Atomic Energy Agency, Ibaraki, 319-1195, Japan
[e] Center for Computational Science and e-Systems, Japan Atomic Energy Agency, Ibaraki, 319-1195, Japan
[f] Research Center for Magnetic and Spintronic Materials, National Institute for Materials Science, 1-2-1 Sengen, Ibaraki, 305-0047, Japan
[g] Japan Synchrotron Radiation Research Institute, Hyogo, 679-5198, Japan

ARTICLE INFO

Handling Editor: Dr A Iranzo

Keywords:
Hydrogen embrittlement
Al–Zn–Mg alloys
Aluminum alloys
X-ray tomography
First-principles calculations

ABSTRACT

Our study investigates how hydrogen trapped at interfaces of $MgZn_2$ precipitates affects hydrogen embrittlement in Al–Zn–Mg alloys. Al–Zn–Mg alloys featuring various aged microstructures were prepared, and their hydrogen embrittlement behaviors were monitored in situ during tensile tests via synchrotron radiation X-ray microtomography. The changes in the interfacial properties of $MgZn_2$ instigated a discernible transition in the quasicleavage and intergranular fractures. First-principles calculations revealed that the hydrogen trapping energy at semicoherent interfaces of $MgZn_2$ is significantly high at 0.56 eV/atom, and multiple hydrogen trapping leads to a substantial reduction in interfacial cohesive energy. Hydrogen partitioning analysis of all trapping sites, including vacancies, grain boundaries, and $MgZn_2$ interfaces, demonstrated that in overaged alloys, more than 90% of the hydrogen was trapped at semicoherent interfaces. The hydrogen trapped at the semicoherent interface of $MgZn_2$ decreased the interfacial cohesive energy, causing semispontaneous decohesion and quasicleavage fracture in the Al–Zn–Mg alloys.

1. Introduction

In structural metals, hydrogen is an undesirable element because of its propensity to segregate at various trapping sites, such as dislocations, vacancies, and grain boundaries, thereby predisposing materials to delayed fracture and stress corrosion cracking [1–7]. Hydrogen embrittlement (HE), which is widely recognized as a critical issue in steels [8–10] and nickel-based alloys [11–13], is an equally severe problem in high-strength aluminum wrought materials, specifically, Al–Zn–Mg alloys [3,14–16]. HE becomes increasingly severe with increasing alloy strength [17]. In practical applications, a common strategy for mitigating HE susceptibility involves intentionally reducing the strength of Al–Zn–Mg alloys through overaging [18]. Overaging induces coalescence and disorder at the coherent interfaces of precipitates, consequently leading to a decrease in the macroscopic strength and an increase in the HE resistance. These changes suggest that the morphology and interface coherency of precipitates exert discernible influences on hydrogen trapping at these sites.

Nevertheless, the fundamental understanding of hydrogen trapping in precipitates during aging remains a subject of debate among researchers [18–24]. After performing tritium autoradiography, Iijima et al. and Young et al. reported that η′ precipitates in Al–Zn–Mg alloys did not trap hydrogen and that the interfaces between η precipitates and the matrix in the grain interior were hydrogen trapping sites [19,20]. Bond et al. reported that hydrogen was trapped near Si-rich or Fe- and Si-rich precipitates, according to the results of secondary ion mass spectrometry [18]. Furthermore, Nguyen et al. concluded from mechanical tests and transmission electron microscopy (TEM) observations

* Corresponding author.
** Corresponding author.
E-mail addresses: ksmz@tottori-u.ac.jp (K. Shimizu), toda@mech.kyushu-u.ac.jp (H. Toda).

https://doi.org/10.1016/j.ijhydene.2025.02.123
Received 30 October 2024; Received in revised form 1 February 2025; Accepted 7 February 2025
Available online 18 February 2025

that grain boundary precipitates were strong hydrogen trapping sites [23].

Hydrogen in structural materials is problematic because it degrades the mechanical properties at the ppm level and is difficult to detect experimentally [25]. Consequently, atomic-scale simulations have emerged as valuable tools for interpreting the role of hydrogen, particularly in the context of HE in steels [26–29]. In 2018, Tsuru et al. performed first-principles calculations for hydrogen trapping at the coherent interfaces of $MgZn_2$ (η precipitates) in aluminum [30]. The scholars found that the coherent interface of $MgZn_2$ was a hydrogen trapping site with a maximum trapping energy of 0.35 eV/atom. Notably, in 2020, Tsuru et al. reported that hydrogen enrichment at the precipitate interface induced semispontaneous decohesion [31]. The term semispontaneous is used here because hydrogen does not completely spontaneously concentrate at the interface but rather aggregates at the interface with the assistance of an external load or stress. Three factors contributed to this phenomenon: the presence of multiple hydrogen traps at the precipitate interface, the low surface energy (0.82 J/m^2 for Al(111) [32]), and the high hydrogen trapping energy at the matrix surface. Metals with high surface energy, such as iron (2.358 J/m^2 for α-Fe(110) [33]), do not exhibit spontaneous decohesion due to the presence of hydrogen [34,35].

Hydrogen is trapped not only in precipitates but also in vacancies, dislocations, and grain boundaries; these trapped hydrogen sites are arguably potential origin sites of hydrogen embrittlement [36]. For example, according to the hydrogen-enhanced localized plasticity mechanism [37], an analysis based on the interaction between hydrogen and the elastic stress field around a dislocation core revealed that hydrogen enhanced dislocation migration [38]. In studies of the hydrogen-enhanced strain-induced vacancy mechanism [39,40], it was reported that hydrogen-trapped vacancies accelerated the agglomeration of vacancies to nucleate nanovoids, resulting in hydrogen-induced cracking. Regarding the mechanism of quasicleavage fracture, considerable research has discussed nanovoid coalescence originating from hydrogen-stabilized vacancies [40], hydrogen-accelerated dislocation processes [41], and a combination of hydrogen-enhanced and hydrogen-reduced dislocation mobility [42].

However, the proposed mechanism for hydrogen-induced quasicleavage cracks could not be interpreted as HE in Al–Zn–Mg alloys because the levels of hydrogen occupation at dislocations and vacancies were found to be lower than those at other hydrogen trapping sites due to their low hydrogen trapping energies [15]. In our previous report, we concluded that hydrogen-induced nanovoids formed in hydrogen-charged Al–Zn–Mg–Cu alloys; however, their coarsening and agglomeration characteristics were limited, and they were not involved in fracture [43]. In addition, because the hydrogen trapping energy of dislocations in aluminum was low, the quasicleavage fracture mechanism based on slip band separation, which has been reported to occur steels and Ni-based alloys, was not considered feasible. Shibata et al. analyzed the crystallographic orientations of the fracture surfaces of hydrogen-charged steels via electron backscattered diffraction (EBSD) and reported that hydrogen-related quasicleavage cracking occurred in the $\{011\}_{BCC}$ plane of steel; these researchers did not observe typical cleavage fractures in the $\{001\}_{BCC}$ plane [44–46]. Zhang et al. crystallographically investigated hydrogen-induced quasicleavage cracking in Ni-based alloys. The researchers reported that hydrogen-induced cracking and separation along dislocation slip bands, i.e., along the $\{111\}_{FCC}$ planes with the highest Schmid factor, led to crystallographic features of quasicleavage fractures [47]. In Al–Zn–Mg alloys, Hirayama et al. analyzed the crystallographic orientations of quasicleavage fractures in high-hydrogen alloys using diffraction contrast tomography [48]. The authors did not observe the formation of quasicleavage fractures at a specific crystallographic plane, indicating that the quasicleavage fracture of Al–Zn–Mg alloys had no crystallographic characteristics, differing from the fracture traits of Ni-based alloys and steels.

Hydrogen trapping and the associated HE behaviors in Al–Zn–Mg alloys are variable and depend on the characteristics of their aged microstructures, particularly the microstructures of their precipitates. In this study, we demonstrate that hydrogen trapping at precipitate interfaces is the dominant factor contributing to HE in Al–Zn–Mg alloys. For this purpose, several Al–Zn–Mg alloys with different microstructures were prepared, and their hydrogen embrittlement behaviors were investigated through in situ tensile testing via synchrotron radiation X-ray tomography. To illustrate that changes in the structures of the precipitate–matrix interfaces could be used to characterize HE behavior, high-angle annular dark-field (HAADF) scanning transmission electron microscopy (STEM) was employed for nanoscale analysis of the coherent interfaces of the precipitates. The hydrogen trapping energy of the $MgZn_2$ semicoherent interface was subsequently ascertained via ab initio calculations involving a model derived from nanoscale observations of the interfacial structure. Finally, hydrogen partitioning in all hydrogen trapping sites, including vacancies, grain boundaries, and $MgZn_2$ coherent and semicoherent interfaces, of the Al–Zn–Mg alloys was quantitatively analyzed. This comprehensive approach was applied to determine the origins of HE in Al–Zn–Mg alloys.

2. Methodology

2.1. Specimens and microstructural analyses

The sample used in this study was an Al–4.0 mol%Zn–2.0 mol%Mg ternary alloy with a Zn/Mg atomic ratio of 2.0. After casting, ingots of this alloy were homogenized at 773 K for 24 h and subsequently subjected to hot and cold rolling until a total reduction of 90% was achieved. The rolled alloy was initially solution treated at 773 K for 1 h and subsequently quenched in ice water. The alloys that were subjected to natural aging were stored at room temperature for 4 days after quenching. The other alloys were artificially aged under various conditions to alter the coherent interfaces and sizes of the precipitates. In this work, the alloys aged at 393 K for 40 h were referred to as PAs, and those that were first aged at 393 K for 40 h and then overaged at 453 K for 1, 7, 35, and 139 h were referred to as OA1, OA7, OA35, and OA139, respectively. The specimens for observation by in situ synchrotron radiation X-ray tomography during tensile testing were machined using electrical discharge machining (EDM). A wire-cut electrical discharge machine in water purified with ion exchange resins was employed. Here, the gauge length of the specimen was 0.7 mm, and the cross-sectional area was 0.6 mm × 0.6 mm. Further details of the specimen geometry are given in the Supplementary Materials (Fig. S1). EDM in water allowed hydrogen charging of the specimens [49]. We used parameters optimized for cutting a 1-mm-thick aluminum sheet. The processing time was approximately 30 min for each specimen. In addition to performing EDM in water, EDM in oil (DAPHNE CUT HL-25, produced by Idemitsu Kosan Co. Ltd.), which prevents the generation of hydrogen from a surface reaction of aluminum with water, was performed to prepare specimens with low hydrogen contents [15]. After performing EDM, the specimens were stored in acetone for at least 4 days to allow hydrogen to diffuse inside the alloy. Assuming that the diffusion coefficient of hydrogen in aluminum at room temperature was 2.3×10^{-11} m^2/s, the diffusion distance after 4 days was estimated to be 2.8 mm [50]. This diffusion distance was greater than the length of one side of the specimens. Moreover, hydrogen was determined to have diffused from the surface to the center of each specimen.

The hydrogen content in the prepared Al–Zn–Mg alloys was measured by a gas chromatography-type thermal desorption analyzer (PDHA-1000, NISSHA FIS, Inc.), which revealed a mean hydrogen content of 13.38 ppm after EDM in water (HH) and 1.70 ppm after EDM in oil (LH) (Fig. S2 in the Supplementary Material). To observe the microstructures of the aged specimens via TEM, the specimens were processed into thin films by using a focused ion beam machine equipped with a Ga ion source (Quanta 3D 200i, Hitachi High-Tech). After

processing, Ar ion milling (NanoMill Model 1040, Fischone) was performed to remove damage and contamination from the specimens. Observations of the aged precipitates were conducted via TEM. HAADF–STEM images were recorded using a 200 kV accelerating voltage double aberration-corrected (image and probe Cs) cold-FEG transmission electron microscope (ARM-200CF, JEOL). The HAADF–STEM image intensity signal was related to the atomic number, thereby facilitating the discrimination between heavy and light elements.

2.2. In situ tensile testing via synchrotron radiation X-ray tomography

Hydrogen embrittlement in Al–Zn–Mg alloys involves complex processes such as plasticity and crack initiation/propagation under external loading. Synchrotron radiation X-ray tomography is an effective analytical tool for investigating these hydrogen embrittlement phenomena. In situ tensile tests were performed at BL20XU in SPring-8. A monochromated X-ray beam with an energy of 20 keV tuned by a Si (111) double-crystal monochromator was applied in this study. The image detector included a 2048 × 2048 element complementary metal–oxide semiconductor (CMOS) camera (ORCA Flash 4.0, Hamamatsu Photonics K.K.), a single-crystal $Gd_3Al_2Ga_3O_{12}$:Ce + scintillator, and an optical lens. The detector was positioned 20 mm behind the specimen. A total of 1800 projections with 180° of scanning in 0.1-degree increments were obtained during each scan. Tomographic image slices were reconstructed from the 1800 projections using a conventional convolutional back-projection algorithm [51], followed by conversion to 8-bit form. During this conversion, the gray values of the 8-bit images were normalized so that the linear absorption coefficients from −30 to 40 cm^{-1} fell within the 8-bit grayscale range from 0 to 255. The isotropic voxel size in the reconstructed images was 0.5 μm, and the spatial resolution of this equipment was reportedly 1.2 μm [52]. After completing the in situ observations, the fracture surfaces of the tested specimens were observed by scanning electron microscopy (SEM).

High-hydrogen Al–Zn–Mg ternary alloys with different aged structures were subjected to tensile testing on an apparatus (CT500, Deben UK Ltd.) with a strain rate of approximately 3×10^{-3} s^{-1}. The influences of aged precipitates on the hydrogen accumulation and partitioning behaviors in Al–Zn–Mg–Cu alloys under monotonic loading were investigated by maintaining a constant displacement of 3.34 ks at each loading step [14,49,53]. In situ observations of each specimen were performed while unloading, at the maximum load, and under a strain of approximately 3%.

2.3. 3D/4D image processing and analysis

To compute parameters such as the volume, surface area, and diameter of the particles and pores with subvoxel accuracy, a marching cube algorithm was applied [54]. To eliminate errors due to image noise, only pores and particles with volumes greater than 9 voxels (1.125 μm^3) were analyzed as microstructural features. Precise 3D image registration was performed to minimize the physical distance between identical particles in images captured at adjacent loading steps. The microstructural feature tracking (MFT) technique, which allows for analysis of deformation behavior, was applied to track all the particles throughout the deformation process [55]. Individual particles were tracked at different loading steps, and their physical displacements were calculated, resulting in a high-density 4D strain map that could directly visualize strain changes in the presence of hydrogen. The details of the microstructural tracking technique and strain mapping are available in the literature [55].

2.4. First-principles calculations for hydrogen trapping

On the basis of HAADF–STEM analysis, we conducted first-principles calculations to investigate hydrogen trapping at $MgZn_2$ semicoherent interfaces. The model construction is directly connected to our experimental observations, its description is given in section 4 and only the computational conditions are described here. The first-principles calculations were performed within the framework of density functional theory (DFT) using the Vienna ab initio simulation package (VASP) [56]. *k*-point sampling of the Brillouin zone was performed using the Monkhorst–Pack algorithm [57]. This algorithm performed 9 × 5 × 5 gamma-centered *k*-point sampling. A first-order Methfessel–Paxton scheme [58] was used with a plane wave energy cutoff of 400 eV and a smearing parameter of 0.1 eV. In all the calculations, the convergence condition for the self-consistent field calculations was an energy difference below 10^{-6} eV. The conjugate gradient method was adopted to explore the relaxed configuration and its energy, where the search was terminated when the force on all the atoms decreased to below 10^{-2} eV/Å.

3. Results

3.1. Microstructure

Fig. 1 shows $MgZn_2$ precipitates in OA1, OA7, OA35, and OA139 using HAADF–STEM. HAADF–STEM observations of PA were previously performed, and the size and interface consistency were reported [59]. Fig. 1 (a), (b), (c), and (d) show HAADF–STEM images of OA1, OA7, OA35, and OA139, respectively, and Fig. 1 (e), (f), (g), and (h) show magnified images of Fig. 1 (a), (b), (c), and (d), respectively. Most $MgZn_2$ precipitated phases in the prepared specimens were disc shaped with orientations of $(0001)_{MgZn_2}//(111)_{Al}$ [60]. The $MgZn_2$ precipitates with this variant included η' ($(10\bar{1}0)_{MgZn_2}//(110)_{Al}$), η_2 ($(10\bar{1}0)_{MgZn_2}//(110)_{Al}$), and η_3 ($(11\bar{2}0)_{MgZn_2}//(110)_{Al}$) phases. With increasing overaging time, the precipitates coarsened, and the average diameter of OA139 reached 27 nm. The coherence analysis results of the precipitate interface were as follows: the OA1 interface was fully coherent, similar to PA; the OA7 interface was coherent at the planar interface on the disc ($(0001)_{MgZn_2}//(111)_{Al}$) and semicoherent at the edge interface on the disc ($(1\bar{1}00)_{MgZn_2}//(\bar{1}10)_{Al}$) or ($(11\bar{2}0)_{MgZn_2}//(11\bar{2})_{Al}$) [60]; and all the OA35 and OA139 interfaces were fully semicoherent. Even after overaging for 139 h, the $MgZn_2$ precipitates were oriented with respect to the matrix, and the interface was semicoherent rather than incoherent. Details of the interface structure identification for OA35 and OA139 can be found in Figs. S3 and S4 in the Supplementary Materials. A summary of the precipitate size and interface coherency characteristics for each aging condition is provided in Table 1.

3.2. Deformation and fracture behaviors in the presence of hydrogen

The changes in the deformation and fracture behaviors were investigated via in situ synchrotron radiation X-ray tomography in specimens with different aging times (PA, OA1, OA7, OA35, and OA139) containing high hydrogen concentrations. Additional testing was conducted on OA7 specimens with a reduced hydrogen content, which were prepared by electrical discharge machining (EDM) in oil rather than water; these specimens are designated OA7 (LH). The mechanical response and resultant fracture surfaces are presented in Figs. 2 and 3, respectively. The periodic drops in the stress–strain curves (Fig. 2) corresponded to stress relaxation during displacement, which is required for tomographic scanning. The stress–strain behavior demonstrated that the PA and OA1 conditions resulted in high strength levels, whereas prolonged overaging led to decreased ultimate tensile strength and increased elongation, which is consistent with typical aging responses in aluminum alloys.

Notably, despite the significant difference in hydrogen content between the OA7(HH) and OA7(LH) specimens (9.6 and 1.7 mass ppm, respectively, as shown in Fig. S2), their fracture elongations were

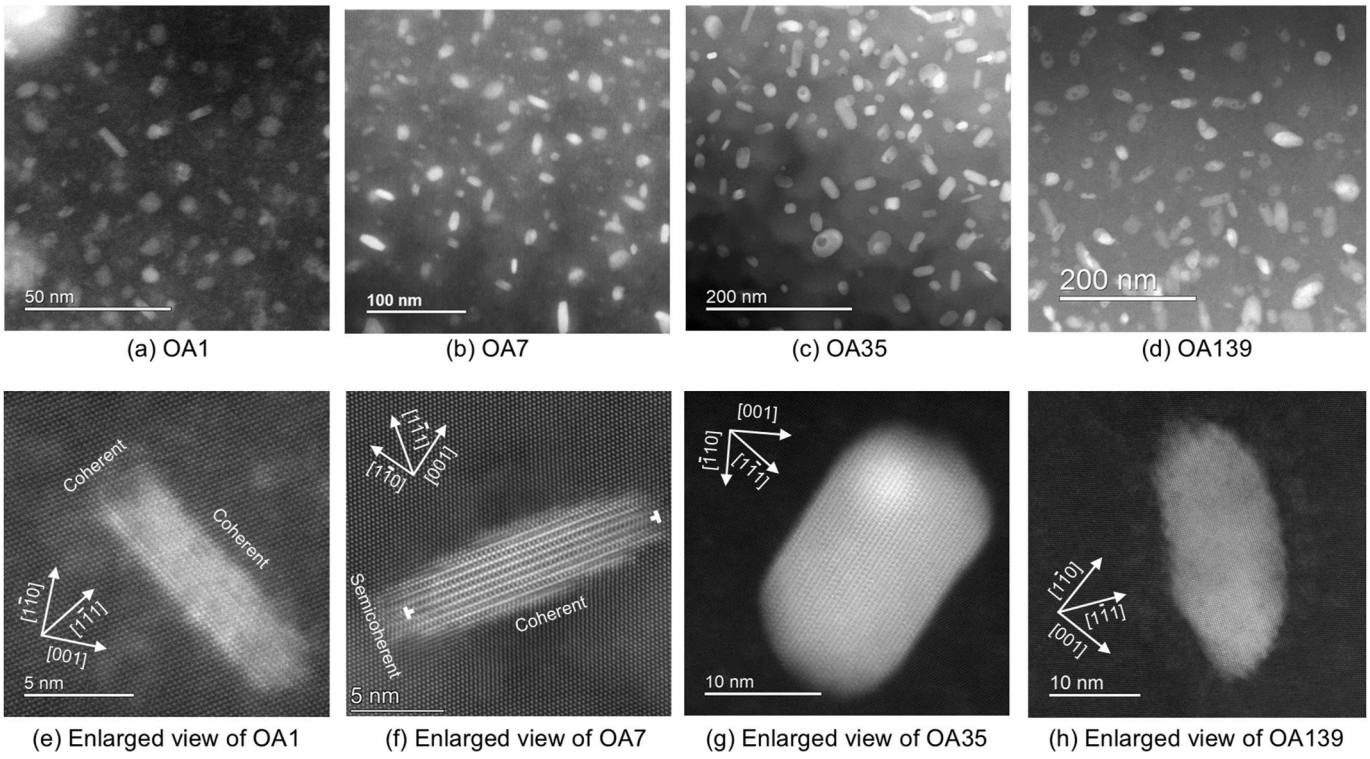

Fig. 1. HAADF-STEM micrographs of $MgZn_2$ precipitates: (a)–(d) low-magnification images of OA1, OA7, OA35, and OA139 specimens, respectively; (e)–(h) corresponding high-magnification images. Note the evolution of interfacial coherency from fully coherent (OA1) to partially semicoherent (OA7) and fully semicoherent interfaces (OA139). For the analysis of the interface structure, see the supplementary material.

Table 1
Summary of the interfacial coherency, size and trapping site density of the precipitate in 1 m^3 of aluminum for each aged specimen.

Specimen	Interfacial coherency	Diameter, d / nm	Thickness, l / nm	Trap site density, N_η / 10^{26}site·m^{-3}	
				Coherent	Semicoherent
PA	Coherent	5	1	5.5	–
OA1	Coherent	7	3	2.5	–
OA7	Coherent and semicoherent	20	5	1.4	0.22
OA35	Semicoherent	23	11	–	0.40
OA139	Semicoherent	27	14	–	0.32

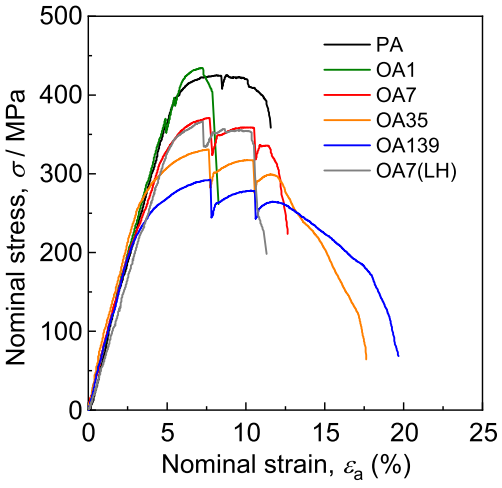

Fig. 2. Nominal stress-strain curves obtained during in situ tensile testing under synchrotron radiation X-ray tomography for PA, OA1, OA7, OA35, OA139, and low-hydrogen OA7(LH) specimens. Vertical load drops indicate stress relaxation during tomographic scanning.

comparable. This observation suggested that the hydrogen embrittlement susceptibility of Al–Zn–Mg alloys was not determined by the total hydrogen content but rather by local hydrogen accumulation at specific microstructural features.

The fractographs presented in Fig. 3(a–f) indicate that only OA1 experienced only intergranular fractures, whereas the other four specimens experienced a combination of intergranular, quasicleavage, and ductile fractures. OA7 had the most apparent quasicleavage fracture, comprising 39% of the total area. The initial cracks in PA, OA7, OA35, and OA139 were all quasicleavage cracks, which were directly identified by superimposing fractographs with crack initiation visualized by in situ tomography (see Fig. S5 in the Supplementary Materials for details).

Fig. 4 (a) and (b) show magnified secondary electron images of OA1, which exhibited the most obvious intergranular fracture. Although the fracture surface of the intergranular fracture, as shown in the low-magnification image in Fig. 3, appeared flat, upon closer examination of the high-magnification images in Fig. 4 (a) and (b), nanodimples with $MnZn_2$ nuclei were found to cover the surface. Notably, the magnified images of Fig. 4 (a) and Fig. 4 (b) revealed dimples with sizes on the order of several hundred nanometers, indicating a clear departure from the dimple size typically associated with ductile fracture (ranging from several microns to several tens of microns). Moreover, $MgZn_2$ itself remained intact, suggesting that the interface of coarse $MgZn_2$ dispersed

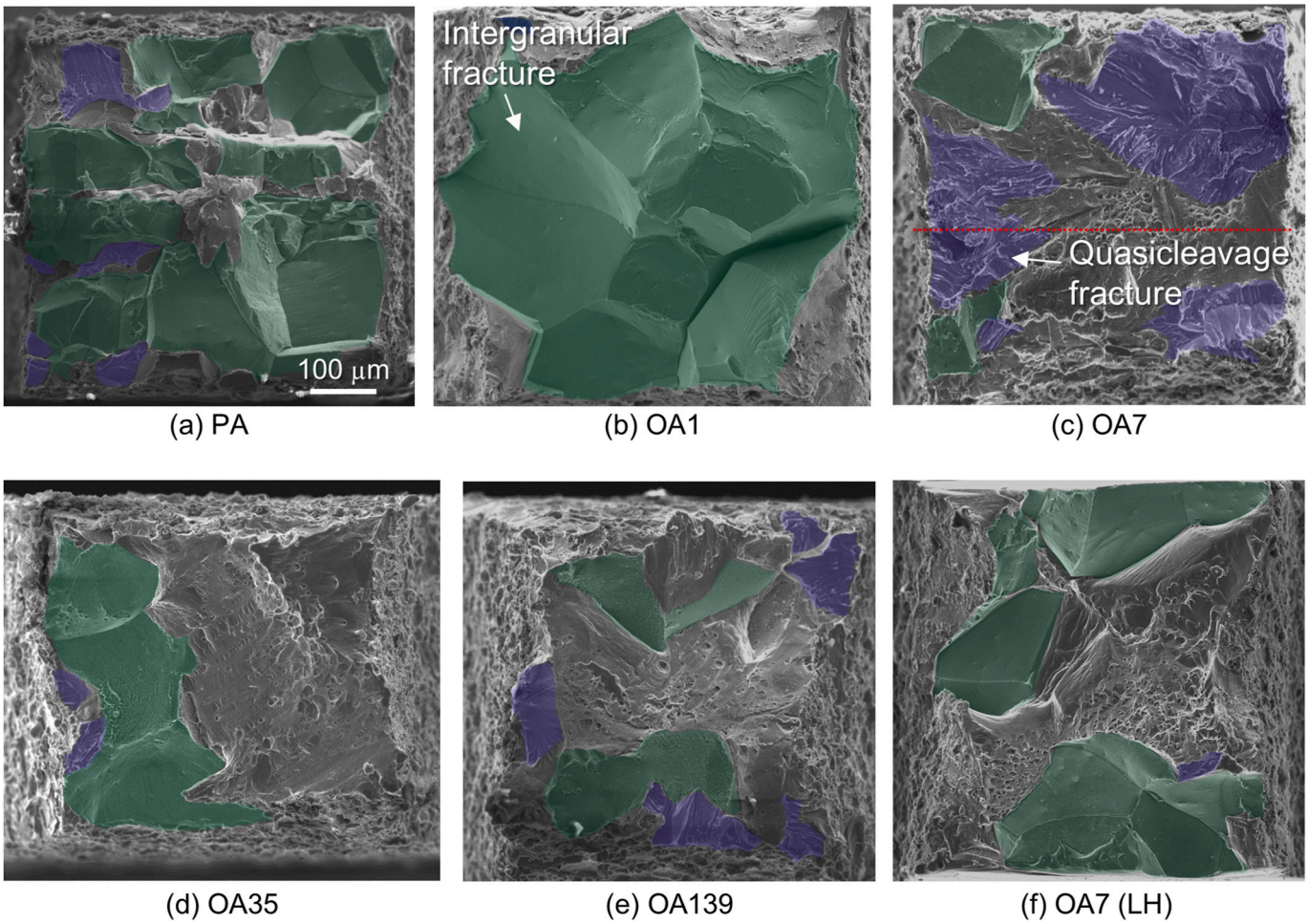

Fig. 3. SEM fractographs after in situ tensile tests: (a) PA, (b) OA1, (c) OA7, (d) OA35, (e) OA139, and (f) OA7(LH) specimens. Regions of intergranular and quasicleavage fractures are highlighted in green and blue, respectively. Note complete intergranular fracture in OA1.

along the grain boundaries was debonded, thus forming intergranular cracks in the form of interconnected nanovoids in the precipitate-free zone. Fig. 4(c) and (d) show magnified images of the fracture surface of OA7, where quasicleavage fracture was most pronounced. In Fig. 4 (c), high-density $MgZn_2$ precipitates were dispersed, as indicated by the yellow arrows, and crater-like decohesion traces with densities similar to those of the precipitates were observed as well, as shown by the light blue arrows. Fig. 4 (d) shows a magnified image of a quasicleavage fracture and shows that the voids originated from precipitate decohesion and were dragged in the undulated region. This local undulation was compatible with the characteristic behavior of quasicleavage fracture, which developed with a reduced level of plasticity.

While hydrogen-induced intergranular fracture mechanisms and their suppression through grain refinement [5,61–63] and micro-alloying [64–66] are well documented, the fundamental mechanisms of quasicleavage fracture—a form of transgranular brittle fracture—are poorly understood in aluminum alloys, particularly in the context of hydrogen embrittlement. In this study, we specifically address the initiation mechanisms of quasicleavage cracking.

Fig. 5 (a), (b), and (c) show that the tomographic slices of OA7, in which the most apparent quasicleavage fracture occurred, were captured at unloading (0% applied strain, ε_a), at 7.7% ε_a, and after fracture, respectively. A quasicleavage crack initiated at 7.7% ε_a before propagating under further monotonic loading to form a fracture surface. This form of crack propagation, which was accompanied by a relatively low level of plasticity, is characteristic of quasicleavage cracks. We previously reported that the crack-tip-opening displacement of a quasicleavage crack in an overaged Al–Zn–Mg alloy was 0.23 μm, and its crack tip remained sharp and advanced without blunting, according to imaging-type synchrotron radiation X-ray tomography [41,53].

3.3. 3D/4D image analysis during deformation

The excess vacancy concentration and dislocation multiplication at 7.7% ε_a (Fig. 5 (b)) could be estimated from the strain components, which were derived via tomographic scanning and subsequent MFT. In the following process, these vacancy concentrations, geometrically necessary dislocation (GND) densities, and statistically stored dislocation (SSD) densities were calculated from the strain components generated by MFT [15,28,50,67]. First, the vacancy concentration under a specific applied strain was expressed as follows [15,28,68]:

$$C_v = \chi \frac{\sigma \Omega_0}{Q_f} \varepsilon_t + C_0 \tag{1}$$

where χ is a dimensionless constant equal to 0.1, σ is the flow stress, Ω_0 is the atomic volume of aluminum, $Q_f = 0.35$ eV is the vacancy formation energy for aluminum in the presence of hydrogen [69], ε_t is the true strain, and C_0 is the initial vacancy concentration, which is the thermal equilibrium concentration at 300 K. The GND density, ρ_{GND}, proposed by Paneda et al., was calculated by the following equation [70]:

$$\rho_{GND} = \frac{\eta^p}{\bar{r} b} \tag{2}$$

where $\bar{r} = 1.9$ is the Nye factor in face-centered cubic alloys, η^p is the

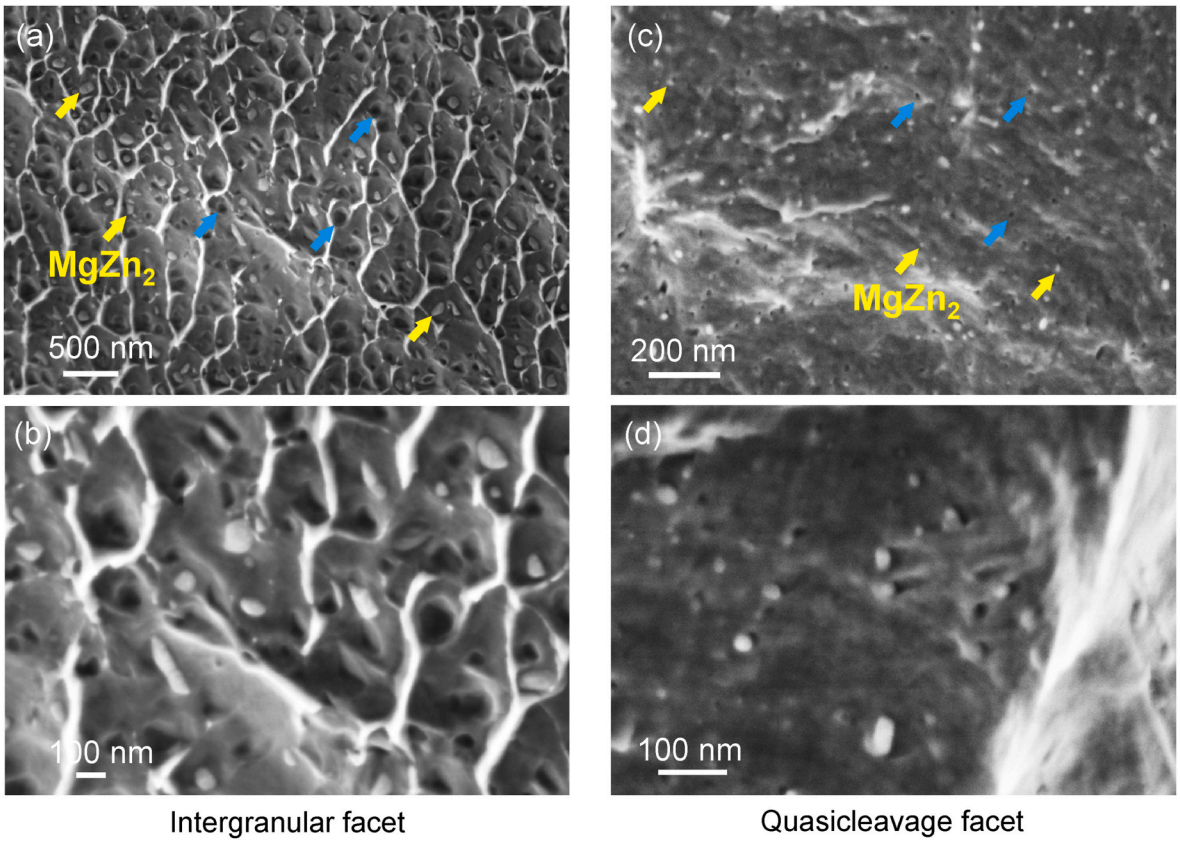

Fig. 4. High-resolution SEM fractographs at low accelerating voltage, showing detailed features from Fig. 3: (a, b) intergranular facets in OA1 specimen and (c, d) quasicleavage facets in OA7 specimen. $MgZn_2$ precipitates (yellow arrows) and crater-like decohesion traces from precipitate interfaces (light blue arrows) were observed. The nano-dimpled morphology suggests precipitate-matrix interface debonding.

equivalent plastic strain gradient, and $b = 0.286$ nm is the magnitude of the Burgers vector. The SSD density, proposed by Brinckmann et al., was calculated by the following expression [71]:

$$\rho_{SSD} = \frac{\sqrt{3}\,\bar{\varepsilon}^{p}}{bl} \tag{3}$$

where $\bar{\varepsilon}^{p}$ is the equivalent plastic strain and l is the mean free path of dislocation motion, which is defined as half of a single dislocation slip distance in the grain interior. Fig. 5 (d), (e), (f), and (g) show 2D cross-sectional maps of the equivalent plastic strain, vacancy concentration, GND density, and SSD density, respectively, at an ε_a value of 7.7% in OA7. The distributions of the vacancy concentration and SSD corresponded to those of the equivalent strain, indicating localization at the center of the gauge. The GND density shown in Fig. 5 (f) was concentrated in the region of a large strain gradient shown in Fig. 5 (d), which resulted in the formation of an isolated region, as shown by the white arrow.

4. Discussion

4.1. Hydrogen trapping at the precipitate interface

An important strategy for understanding hydrogen-induced intergranular and quasicleavage cracking is by performing a comprehensive evaluation of the partitioning characteristics of hydrogen in materials. Hydrogen is partitioned to specific types of sites, such as vacancies and dislocations, depending on their trapping energies and trapping site densities [50]. The hydrogen trapping energies of all the sites, such as Mg solutes [31], vacancies [72], dislocations [73], pore surfaces (aluminum surfaces) [74], grain boundaries [32], and coherent interfaces of the $MgZn_2$ precipitates [30], have been reported for aluminum, but those of the semicoherent interfaces of the $MgZn_2$ precipitates remain unknown. The difficulty in modeling arises from the periodic boundary conditions and the number of atoms involved in deriving the hydrogen trapping energy at the $MgZn_2$ semicoherent interface through first-principles calculations.

However, we have revealed in this study that the significance of hydrogen trapping at the semicoherent $MgZn_2$ interface and its hydrogen-induced decohesion in the HE of Al–Zn–Mg alloys, particularly during quasicleavage fracture. Therefore, while absolute reliability could not be guaranteed, as a practical approach, we conducted first-principles calculations on the hydrogen trapping behavior at the semicoherent interface. On the basis of crystallographic analysis of the HAADF–STEM observations presented in Fig. 1 and previously reported crystallographic relationships of $MgZn_2$ precipitates [75], we constructed atomic models of the semicoherent interfaces. The interface models were designed with the semicoherent boundary oriented perpendicular to the coherent interface plane, comprising nine Al(111) atomic layers interfaced with ten $MgZn_2$(0001) layers. The dimensions of the $MgZn_2$(0001)-2.5 unit and Al(111)-3 unit models were derived from experimental TEM observations to periodically minimize the strain. Although assessments based on energy considerations such as coherency were not feasible, we anticipated reasonable results for our hydrogen trapping investigations.

The aluminum and $MgZn_2$ precipitates had a face-centered cubic structure and a C14 Laves phase (space group $P6_3/mmc$) [76], respectively. Atomic models of an interface with orientations of $(11\bar{2}0)_{MgZn_2}//(11\bar{2})_{Al}$ and $(1\bar{1}00)_{MgZn_2}//(\bar{2}10)_{Al}$ after structural relaxation were drawn by using Visualization for Electronic and STructural Analysis (VESTA) software [77] and are shown in Fig. 6 (a) and (b),

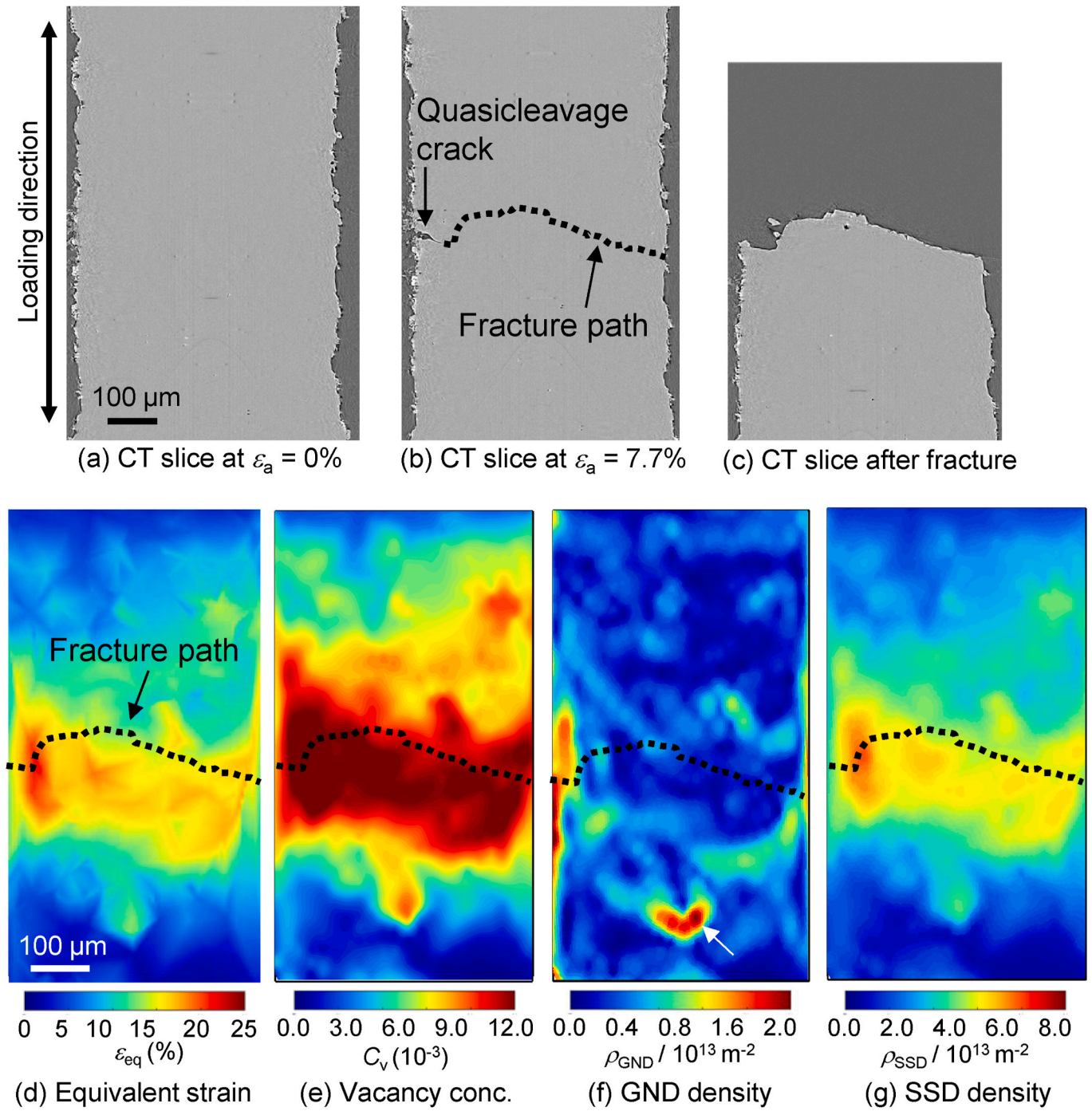

Fig. 5. (a–c) Tomographic slices and developmental behavior of (d) equivalent strain, (e) vacancy concentration, and (f) GND and (g) SSD densities at the applied strain of 7.7% in the OA7 specimen. vacancy concentration, GND and SSD densities were calculated from the strain components in (d). The fracture path is shown as the black dashed line in (b, d-g). The geometric positions of these cross-sectional images correspond to the red dashed lines in Fig. 3 (c).

respectively. A semicoherent interface perpendicular to the coherent interface was constructed as the boundary between nine Al (111) layers and ten $MgZn_2$ (0001) layers. The lattice mismatch was expected to be extremely small based on the lattice parameters of each crystal. While additional orientation relationships exist for $MgZn_2$ semicoherent interfaces beyond the two, our computational analysis was constrained by resource limitations. Fig. 6(a) and (b) represent large-scale atomic models comprising 396 and 228 atoms, respectively. Given the computational capacity constraints, our research focused on the two interface configurations observed experimentally in Fig. 1.

In Fig. 6(a) and (b), there was one interfacial dislocation in $MgZn_2$ for 9 layers of Al(111) that could minimize the total energy of the system. In this cell, the $MgZn_2$ crystal side did not satisfy the periodic boundary condition, and a fixed edge was applied along the <111>// <0001> direction, as shown in the small dark gray spheres in Fig. 6(a) and (b). As illustrated in Fig. 6(a) and (b), we introduced interfacial dislocations into the model by restricting the atomic degrees of freedom near the cell boundaries. The small dark gray spheres represented these constrained atoms. Specifically, these atoms were fixed along the interface plane but allowed to move freely in the c-axis direction perpendicular to the interface plane. We initially expressed concern that this constrained region could artificially inflate hydrogen trapping

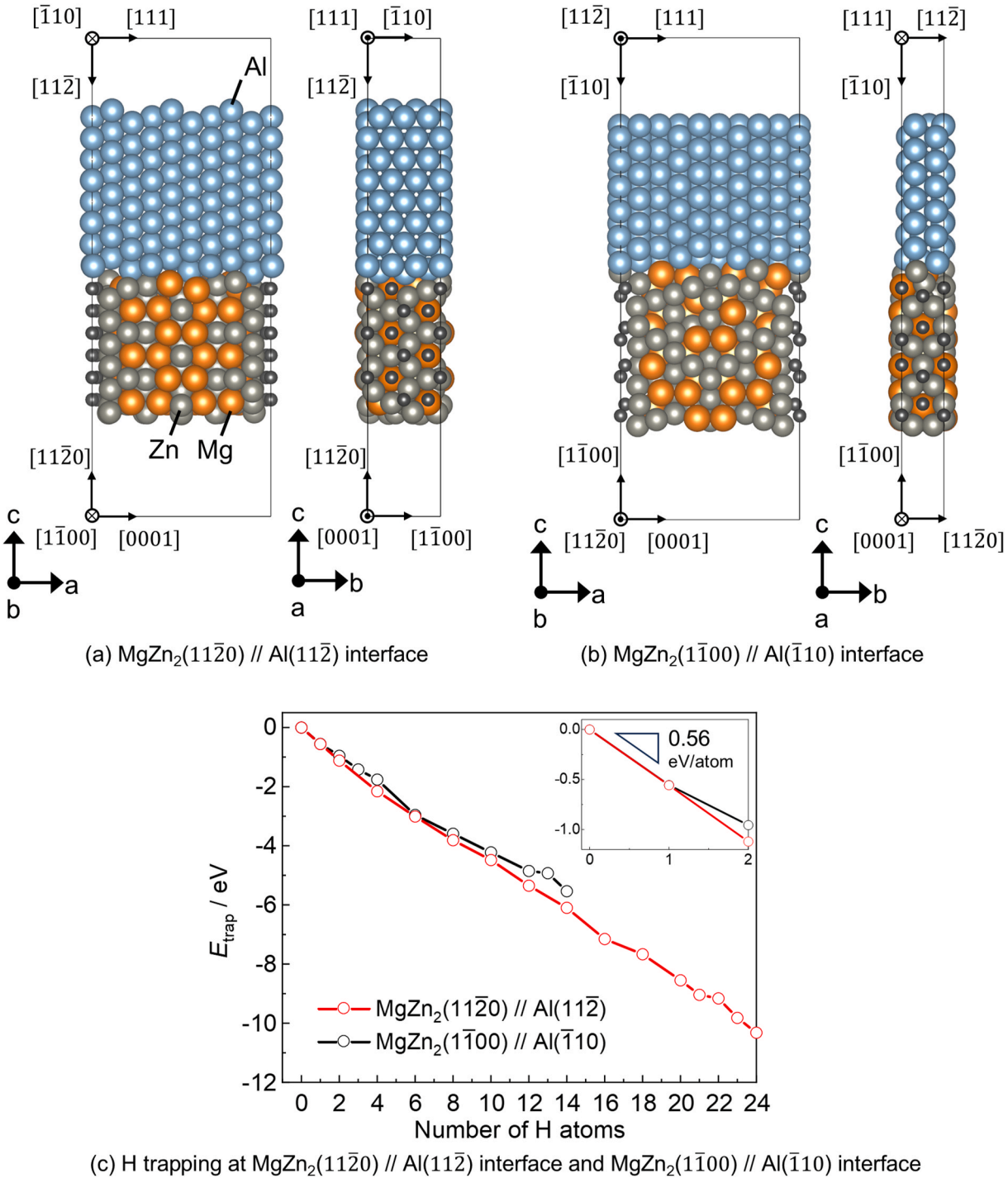

Fig. 6. Modeling of MgZn, semicoherent interfaces and calculation of multiple hydrogen trapping at the interface. (a) $(11\bar{2}0)_{MgZn_2}//(11\bar{2})_{Al}$ interface and (b) $(1\bar{1}00)_{MgZn_2}//(\bar{1}10)_{Al}$ interface after structural relaxation. Due to the introduction of the interface dislocation which is located in the center of the model, the atoms located at the edges of $MgZn_2$, shown as small spheres, had their horizontal displacements fixed. (c) calculation of multiple hydrogen trapping at semi-coherent interfaces.

energies. However, a previous report suggested a minor impact from such constraints [78]. This phenomenon could be attributed to the maintained atomic mobility in the c-axis direction.

Using the structurally relaxed semicoherent interfacial model shown in Fig. 6 (a) and (b), all potential trapping sites at the interface were explored exhaustively. As shown in Fig. 6(c), the energy at which a single hydrogen was trapped in the calculation cell at either of the two semicoherent interfaces was 0.56 eV/atom. This value was suggestive of the fact that the hydrogen trapping energy of the semicoherent interface was much greater than that of the coherent interface, which reached 0.35 eV/atom [30]. This difference was attributed to the fact that the free volume of the interstitial sites at the semicoherent interface, which included the presence of interfacial mismatch, was larger than that at the coherent interface. As shown in Table 2, the trapping energies of specific sites in aluminum were reported to be 0.29, 0.18, 0.11, 0.23–0.27, 0.08–0.35, and 0.70 eV/atom at vacancies, edge dislocations,

Table 2
Trapping energy of each hydrogen trapping site in Al–Zn–Mg alloys.

Trap site	Trap energy, E_{Ti} / eV·atom^{-1}	Ref.
Solute Mg	0.12	[31]
Edge dislocation	0.18	[73]
Screw dislocation	0.11	[73]
Vacancy	0.29	[72]
GB	0.23–0.27	[32]
Coherent interface of $MgZn_2$	0.08–0.35	[30]
Semicoherent interface of $MgZn_2$	0.56	This work
Pore (aluminum surface)	0.70	[74]

screw dislocations, grain boundaries, $MgZn_2$ coherent interfaces, and pore surfaces, respectively [30,32,72–74]. The trapping energy at the semicoherent interface of 0.56 eV/atom was the second largest value after that of the pore surface.

The interfacial site where the hydrogen trapping energy was 0.56 eV/atom had several equivalent sites in the semicoherent interfacial model. We thereby calculated multiple hydrogen traps at these sites by dispersing H atoms so that H–H repulsion rarely occurred. The calculated change in hydrogen energy in multiple hydrogen traps is shown in Fig. 6 (c). The results indicated that hydrogen could be stably trapped multiple times at the interface of the computational cell while maintaining a high trapping energy. As we mentioned earlier, the calculation model used in Fig. 6 was not perfect in terms of validity because periodic boundaries could not be used; nevertheless, it was determined to be sufficient for the discussion of hydrogen trapping.

4.2. Hydrogen-induced debonding at semicoherent interfaces

The interfacial decohesion observed between the $MgZn_2$ precipitates and the matrix (Fig. 4) could be attributed to a hydrogen-induced reduction in the interfacial cohesive energy. To elucidate this phenomenon, we estimated the reduction in interfacial cohesive energy due to hydrogen trapping at two distinct semicoherent interfaces. First-principles calculations were performed to determine the multiple hydrogen trapping energies at the interfaces shown in Fig. 6 and the subsequent hydrogen trapping energies at the Al and $MgZn_2$ fracture surfaces following interfacial separation.

The multiple hydrogen trapping energies at the semicoherent interfaces illustrated in Fig. 6 were converted to corresponding reductions in interfacial energy, and the results are presented in Fig. 7(a). Our previous analysis of coherent interface separation established that hydrogen trapping approached saturation at a density of approximately 20 atoms/nm^2, corresponding to an interatomic hydrogen spacing of 0.2 nm [31]. However, the computational limitations imposed by the extensive unit cell dimensions required for the semicoherent interface atomic model precluded calculations at hydrogen trap densities approaching 20 atoms/nm^2. Therefore, we employed a linear approximation for the interfacial energy reduction, assuming a constant hydrogen trapping energy, as indicated by the slope in Fig. 6(c) and shown in Fig. 7(a). This linear relationship was denoted as $\Delta E_{int}(\rho)$, where ρ represents the trapped hydrogen atom density at the $MgZn_2$/Al interface.

We subsequently evaluated the surface energy reduction induced by multiple hydrogen traps at the Al and $MgZn_2$ fracture surfaces. While relatively large unit cells were necessary to minimize lattice misfit in the semicoherent interface calculations shown in Fig. 7(a), small periodic unit cells could adequately represent the surface structures. Consequently, calculations were performed using cells approximately 1/4 and 1/2 the area of the semicoherent interface for the aluminum and $MgZn_2$ surfaces, respectively, as illustrated by the atomic models in Figs. 7(b-1) and Fig. 7(c-1). To determine the surface energy reduction, we first mapped the hydrogen trapping energies by systematically varying the hydrogen atom positions across the surfaces to identify the most energetically favorable trapping sites. These mapping results are presented in Figs. 7(b-1) and (c-1). Guided by these trapping energy maps, we progressively increased the number of trapped hydrogen atoms to maximize the surface energy reduction, and we calculated multiple hydrogen trapping energies. The results for the Al and $MgZn_2$ fracture surfaces are shown in Figs. 7(b-2) and (c-2), respectively. The calculations were extended until hydrogen surface adsorption reached saturation in both cases. These energy reductions were expressed as functions of the hydrogen atomic surface density $\rho_{Al}(\rho_{MgZn2})$, denoted as $\Delta E^{Al}_{surf}(\rho_{Al})$ and $\Delta E^{MgZn_2}_{surf}(\rho_{MgZn_2})$ for the respective surfaces.

The interfacial cohesive energy in the absence of hydrogen, $E_{coh}(0)$, was calculated from the energy increase associated with separating the Al and $MgZn_2$ blocks by 1.5 nm across the interface in the cell model shown in Fig. 6(a) and (b). The calculated values were 1.26 and 1.17 J/m^2 for the $MgZn_2(1\bar{1}00)//Al(\bar{1}10)$ and $MgZn_2(11\bar{2}0)//Al(11\bar{2})$ interfaces, respectively. The hydrogen-dependent interfacial cohesive energy, $E_{coh}(\rho)$, was then determined by subtracting the hydrogen-induced reduction in interfacial energy (Fig. 7(a)) from $E_{coh}(0)$ and adding the surface energy reductions of the two fracture surfaces (Figs. 7 (b-2, c-2)), yielding the following expression:

$$E_{coh}(\rho) = E_{coh}(0) - \Delta E_{int}(\rho) + \Delta E^{Al}_{surf}(\rho_{Al}) + \Delta E^{MgZn_2}_{surf}(\rho_{MgZn_2}) \quad (4)$$

In this formulation, the sum of the trapped hydrogen densities at the two fracture surfaces ($\rho_{Al} + \rho_{MgZn_2}$) equals the trapped hydrogen density at the semicoherent interface ρ. In addition, hydrogen was allocated to the two fracture surfaces to minimize the cohesive energy.

A schematic of the calculation according to Eq. (4) and the calculated decrease in the interfacial cohesive energy due to hydrogen are shown in Fig. 8(a) and (b), respectively. Hydrogen trapping at the interfaces resulted in significant reductions in cohesive energy: 39% for the $MgZn_2(1\bar{1}00)//Al(\bar{1}10)$ interface and 82% for the $MgZn_2(11\bar{2}0)//Al(11\bar{2})$ interface at a 20 atom/nm^2 hydrogen trap density. These substantial reductions were comparable to our previous findings for coherent interfaces, where the cohesive energy approached zero [31]. While some uncertainty was present in the computational accuracy due to the assumed semicoherent interface structure and constrained atomic degrees of freedom imposed to maintain structural stability, the calculations nonetheless demonstrated the potential for a significant hydrogen-induced reduction in interfacial cohesive energy. Although the reduction in cohesive energy due to hydrogen trapping alone was insufficient to induce spontaneous interfacial decohesion, interfacial separation occurred under applied tensile stress in practical situations. Therefore, the substantial hydrogen-induced reduction in interfacial cohesive energy likely significantly promoted interfacial decohesion under external loading.

This study focuses on the reduction in interfacial cohesive energy at semicoherent interfaces of $MgZn_2$ precipitates dispersed within the matrix. The associated fracture mode is quasicleavage fracture. As shown in Fig. 3(c) and (f), OA7 exhibited decreased quasicleavage fracture under low-hydrogen conditions. However, intergranular fracture was greater in OA7(LH) than in OA7(HH). While hydrogen is a known embrittling element for aluminum grain boundaries [1,32], the intergranular fracture trends observed in Fig. 3 could not be explained by hydrogen effects alone. Given the limited number of crystal grains in the gauge section of our test specimens, the intergranular fracture behavior was considered to be influenced by the grain boundary characteristics, including the misorientation between adjacent grains, tilt angle relative to the loading direction, and precipitate-free zones [48].

4.3. Hydrogen partitioning at different aged microstructures

The hydrogen within the material partitioned not only to the precipitates but also to various other trapping sites. A comprehensive discussion of hydrogen partitioning and HE in alloys is presented in this section. In this study, hydrogen partitioning in Al–Zn–Mg alloys with

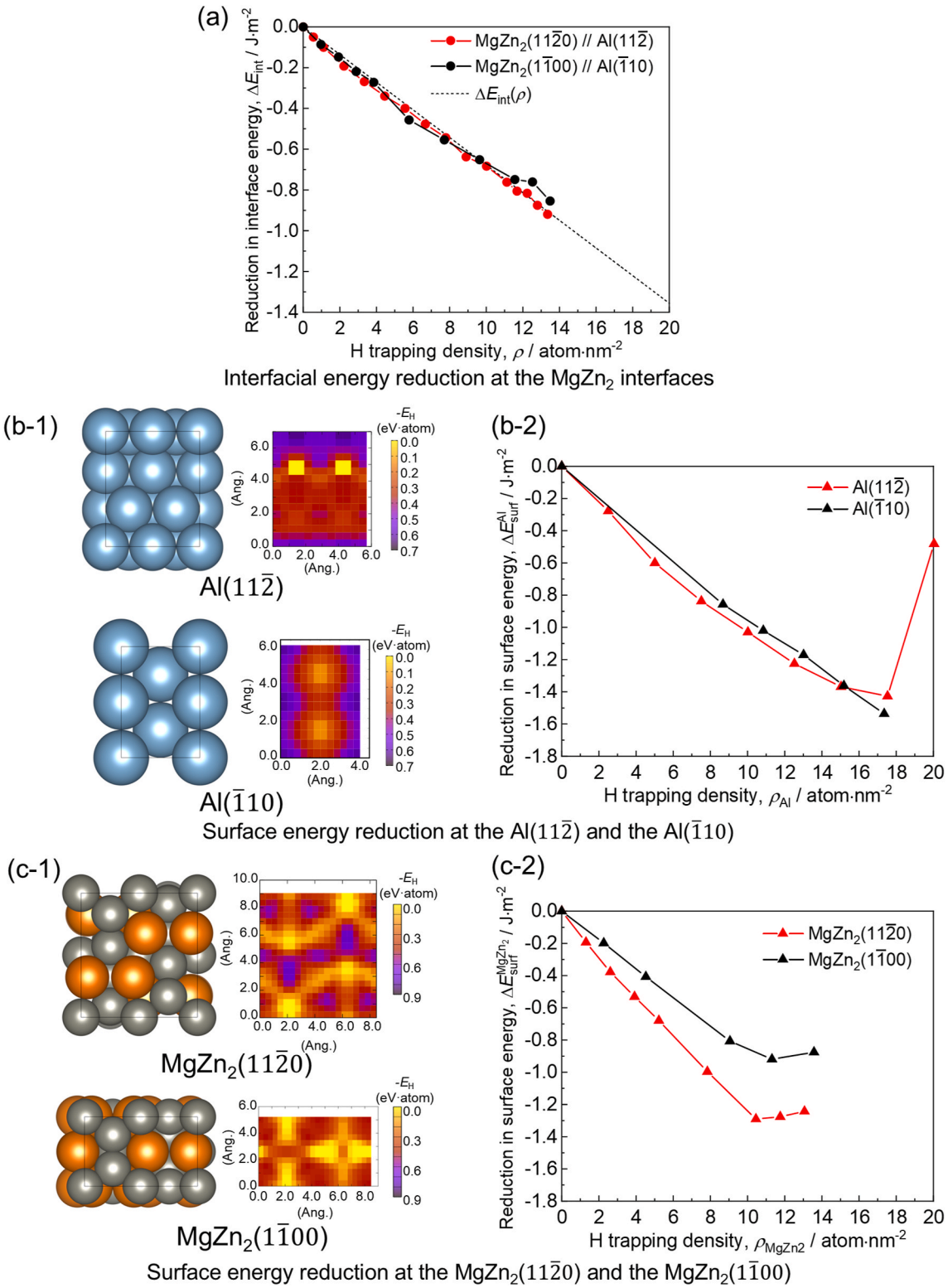

Fig. 7. First-principles calculations of hydrogen-induced energy reductions at interfaces and surfaces. (a) Interfacial energy reduction, ΔE_{int}, at $MgZn_2$/Al semi-coherent interfaces as a function of hydrogen trapping density. (b-1) hydrogen trapping energy contour maps at aluminum surfaces and (b-2) corresponding surface energy reduction, ΔE^{Al}_{surf}, due to multiple hydrogen trapping; (c-1) Al hydrogen trapping energy contour maps at $MgZn_2$, surfaces and (c-2) corresponding surface energy reduction, $\Delta E^{MgZn_2}_{surf}$ due to multiple hydrogen trapping. All energy reductions are quantified as functions of trapped hydrogen density, while the contour maps illustrate the spatial distributions of hydrogen trapping energies across each surface.

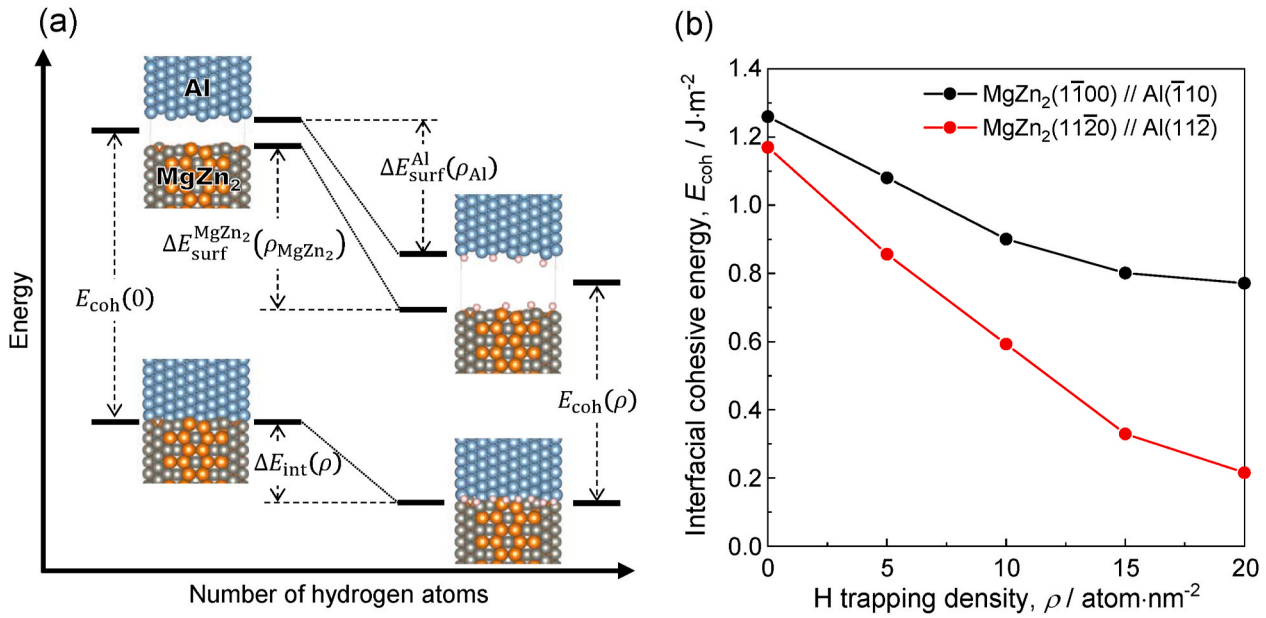

Fig. 8. Hydrogen-induced reduction of interfacial cohesive energy at the $MgZn_2$ semicoherent interface. (a) schematic and (b) results for the calculation of interfacial cohesive energy and its change with hydrogen (indicated by small spheres). The quantification is derived from first-principles calculations incorporating both the hydrogen-mediated decrease in $MgZn_2$, interfacial energy and the concomitant reduction in surface energies of alumimum and $MgZn_2$, as presented in Fig. 7. Results demonstrate 39% and 82% reductions for $MgZn_2(1\bar{1}00)//Al(\bar{1}10)$ and $MgZn_2(11\bar{2}0)//Al(11\bar{2})$ interfaces, respectively, at 20 atoms/nm^2.

different aged microstructures was quantitatively analyzed via Eq. (5) [15,50]:

$$C_H^T = \theta_L N_L + \sum \theta_{Ti} N_{Ti} + C_{pore} \quad (5)$$

where C_H^T is the total hydrogen content in the specimen, N_L is the trap density in the normal interstitial lattice, which corresponds to the number density of tetrahedral sites, N_{Ti} is the trap density in the ith trapping site (excluding micropores), and C_{pore} is the hydrogen content in the pores. Here, the N_{Ti} of dislocations was considered the sum of the SSD and GND densities [15]. The hydrogen occupancy at each trapping site was calculated by assuming that hydrogen atoms trapped at normal interstitial lattices, θ_L, and at other trapping sites, θ_{Ti}, were in thermal equilibrium, as proposed by Oriani [79]:

$$\frac{\theta_{Ti}}{1-\theta_{Ti}} = \theta_L \exp\left(\frac{E_{Ti}}{k_b T}\right) \quad (6)$$

where E_{Ti} is the trapping energy of hydrogen at each site, as shown in Table 2; k_b is Boltzmann's constant; and T is the absolute temperature. The trapping site densities for the precipitates were as described in the previous section, and those at the coherent and semicoherent interfaces of the precipitates per unit volume are summarized in Table 1. The trapping site densities of the vacancies and dislocations were derived experimentally from the analyzed maps shown in Fig. 5(e–g). The total volumes and total surface areas of the pores were measured from 3D tomographic images, and the solute Mg and grain size parameters were analyzed via SEM–EDS and optical microscopy, respectively. The only variable in Eqs. (5) and (6) was θ_L, which could be calculated numerically by incorporating the physical constraint of θ_L ($0 < \theta_L < 1$) [15,50].

Fig. 9 shows the hydrogen partitioning both in the unloading region and in the region ahead of the quasicleavage crack tip (20 μm in diameter from the crack tip in Fig. 5 (b)) at an applied strain of 7.7% in OA7. As shown in Fig. 9 (a), hydrogen was trapped mainly at the coherent and semicoherent interfaces of $MgZn_2$ and the pores because of their high trap densities and hydrogen trapping energies upon unloading. As the strain level increased, excess vacancies and dislocations accumulated in the strain-localized region ahead of the crack tip, and hydrogen atoms were trapped mainly in the vacancies, precipitate interfaces, and pores. However, Fig. 9 (b) shows that the hydrogen occupancy of the vacancies, i.e., the trapped hydrogen content in a vacancy, was low even after deformation. This finding (the low occupancy of the vacancies) agreed with the results of our previous papers [43,67]; thus, we concluded that nanovoids were not the dominant factor for HE in Al–Zn–Mg alloys, as discussed at the latter part of introduction. Like vacancies, dislocations were localized to crack tips after deformation. Nonetheless, the increase in the amount of hydrogen trapped at dislocations was slight due to the low trapping energy of 0.18 eV/atom for edge dislocations with hydrostatic stress fields in the dislocation core. As shown in Fig. 9 (a), the amount of hydrogen trapped in the pores was the second highest after the semicoherent interface of $MgZn_2$; the pores were filled with hydrogen gas, and hydrogen was adsorbed at trapping sites on their inner surfaces [74]. Pores that were 1–3 μm in size and dispersed at nearest neighbor distances ranging from tens to hundreds of μm contributed to ductile fracture, which was dominated by the coalescence and growth of voids and pores at the micron level [80]; however, it was relatively difficult for pores to contribute to HE, a process in which hydrogen-induced crack initiation and growth are considered crucial.

The most important hydrogen partitioning behavior shown in Fig. 9 (a) and (b) was hydrogen trapping at the semicoherent interface of $MgZn_2$. Notably, 91% of the total trapped hydrogen was partitioned there, and the hydrogen occupancy of the semicoherent interface was fairly high. This result suggested that the semicoherent interface was a major hydrogen trapping site in the overaged Al–Zn–Mg alloys.

From the results shown in Fig. 9 (b), when comparing the hydrogen partitioning of alloys in different aging states, hydrogen partitioning during unloading was determined to be sufficient. As in OA7, hydrogen partitioning calculations without loading were conducted for PA and OA139, and the results for the hydrogen occupancy of each site are shown in Fig. 10. The absence of semicoherent precipitates in PA resulted in higher hydrogen occupancy at several sites, such as the coherent interfaces of $MgZn_2$ and vacancies, than that of the overaged specimens. The hydrogen occupancy at the precipitate interface was highest in OA7. In OA139, as shown in Table 1, the entire precipitate interface was semicoherent, resulting in a high trapping site density at the semicoherent interface, and the hydrogen occupancy at the

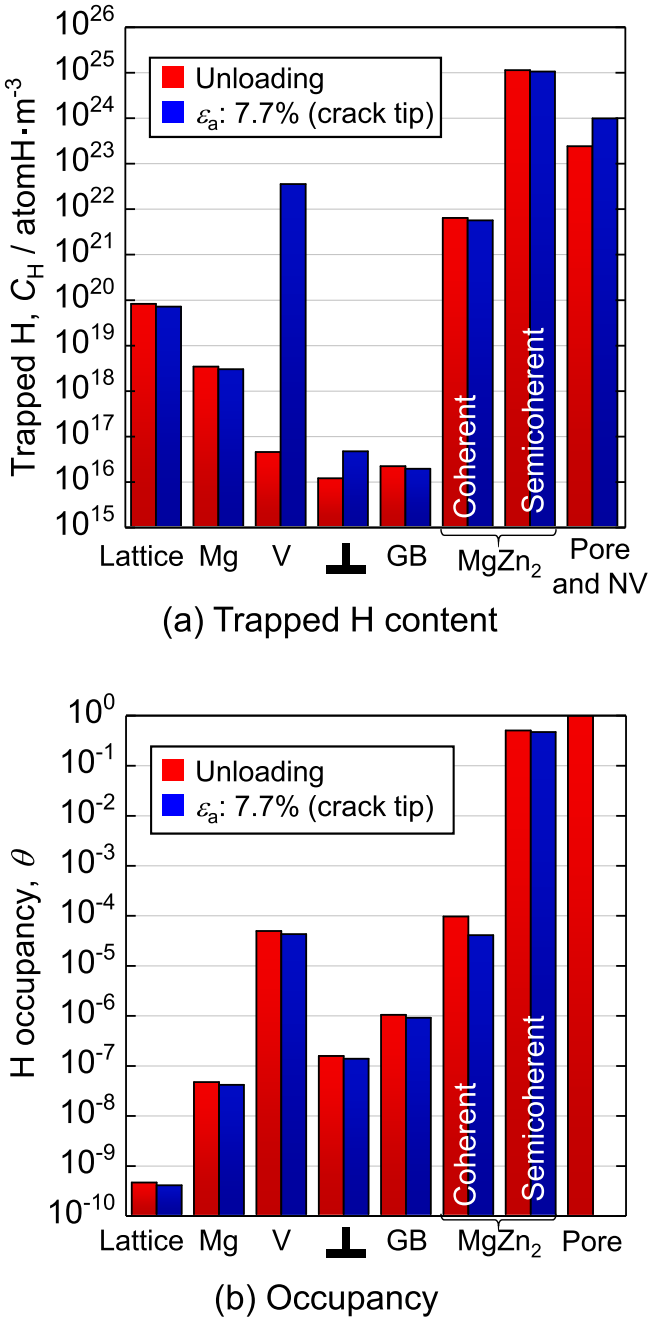

Fig. 9. Hydrogen partitioning behavior in OA7 specimen: (a) trapped hydrogen content and (b) hydrogen occupancy at various trapping sites, comparing distributions in unloaded state and at crack tip region (7.7% strain). Note dominant hydrogen segregation at semicoherent interfaces.

semicoherent interface was lower than that in OA7. In PA, OA7, and OA139, the hydrogen occupancy at the precipitate interface was the second highest after that of the pores. The hydrogen occupancies at the precipitate interfaces of PA, OA7, and OA139 were 4.2×10^{-2} (coherent), 5.0×10^{-1} (semicoherent) and 3.4×10^{-1} (semicoherent), respectively. As mentioned in the introduction, when the hydrogen occupancy at the $MgZn_2$ coherent interface increased, the hydrogen decreased the interfacial cohesive energy and caused semispontaneous debonding of the interface, thus inducing quasicleavage fracture [31].

4.4. Hydrogen partitioning during relevant HE behavior

In this section, macroscopic quasicleavage and intergranular fracture behaviors are discussed in terms of hydrogen occupancy. In various aged states, the area fractions of quasicleavage and intergranular fractures were measured from the fractographs shown in Fig. 3 and rearranged as functions of hydrogen occupancy at the grain boundaries and precipitate interfaces, as displayed in Fig. 11. Fig. 11 (a) shows that the higher the hydrogen occupancy of the precipitate interface was, the greater the fraction of quasicleavage fracture. In particular, for OA7, the hydrogen occupation at the semicoherent interface was high because the area of the semicoherent interface was limited to the edge plane of a disc-shaped precipitate, which resulted in the most pronounced quasicleavage fracture in the prepared Al–Zn–Mg alloys. Both the fractographs shown in Fig. 4(c) and (d) and the perspective of hydrogen partitioning shown in Fig. 11(a) suggest that there was no contradiction between the interface decohesion of precipitates originating from hydrogen trapping at the precipitate interface and the quasicleavage fracture tendency. Furthermore, prolonged overaging reduced the area fraction of quasicleavage fracture, as shown in Fig. 3, which was consistent with the suppression of HE by overaging described in the introduction [10].

Our analysis revealed that the morphologies and densities of precipitates, along with the presence or absence of coherent and semicoherent interfaces, were insufficient for assessing the susceptibility to quasicleavage fracture. The critical factor was the hydrogen occupancy at specific interfacial sites. Specifically, OA7 had a unique characteristic: a limited number of semicoherent interfaces with high hydrogen trapping energy (Fig. 1 and Table 1), coupled with notably high hydrogen occupancy at the $MgZn_2$ interface (Fig. 10). This characteristic distinguished OA7 from PA and OA139, directly contributing to its increased susceptibility to quasicleavage fracture. Compared with OA7, OA35 had a lower hydrogen occupancy at the semicoherent $MgZn_2$ interface (Fig. 10), which substantially decreased its propensity for quasicleavage fracture.

According to the hydrogen occupancy at the grain boundary indicated by the vertical axis in Fig. 11 (a) and (b), there was a very weak correlation between the hydrogen occupancy of the grain boundaries and the fractional areas in both the quasicleavage and intergranular fractures. Yamaguchi et al. discovered via first-principles calculations that hydrogen enrichment at grain boundaries induced interfacial separation (intergranular fracture) and $MgZn_2$ precipitate interfaces [32]. However, the hydrogen trapping energy of the aluminum grain boundaries was less than 0.3 eV/atom, despite the presence of high-energy grain boundaries, such as Σ5(012), which was lower than that of precipitate interfaces. The hydrogen in aluminum was preferentially trapped at the precipitate interfaces, making the direct accumulation of a high amount of hydrogen at the grain boundaries energetically unfeasible in the Al–Zn–Mg alloys. As shown in Fig. 4(a) and (b), it was reasonable that interfacial debonding of $MgZn_2$ precipitates was involved in intergranular fracture. In the hydrogen partitioning analysis conducted in this study, specific features near grain boundaries, such as the coherent interface of a precipitate and the presence of a precipitate-free zone, were not considered. Therefore, accurate hydrogen partitioning at grain boundaries has yet to be performed. Although the possibility of hydrogen inducing debonding of grain boundary precipitate interfaces has been suggested for intergranular fracture, as indicated in Fig. 3(f), the occurrence of intergranular fracture even under low hydrogen contents suggests that elucidating the origins of intergranular fracture remains a challenge to be solved in the future.

Fig. 12 shows a quasicleavage cracking model of Al–Zn–Mg alloys considering hydrogen accumulation at the precipitate interface. As illustrated in Fig. 12 (a), hydrogen accumulation at limited semicoherent interfaces, such as OA7 in this study, drastically reduced the interfacial cohesive energy and caused hydrogen-induced interface decohesion, culminating in quasicleavage cracking. A critical consideration in our research is the absence of direct evidence showing how precipitate interface cracks interconnect to form quasicleavage fracture surfaces. However, our analysis of quasicleavage fracture in Al–Zn–Mg

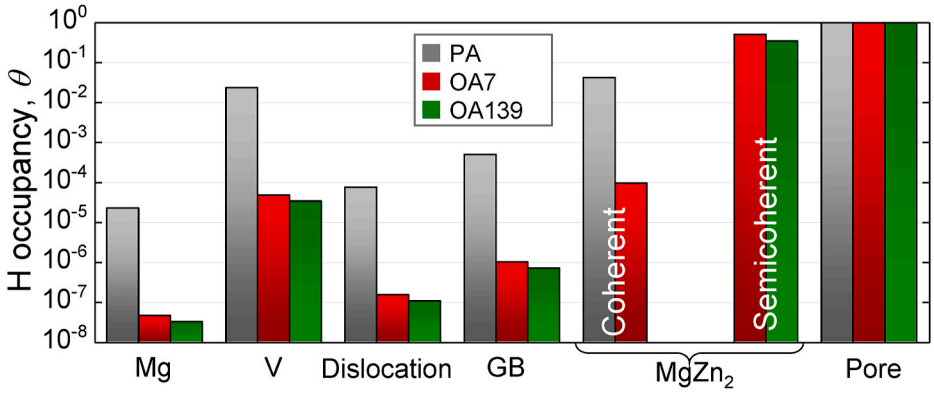

Fig. 10. Hydrogen partitioning in three specimens with different aged states, showing the hydrogen occupancy of each trapping site in PA, OA7, and OA139 at the unloaded state. The H occupancy in OA7 is identical to that in Fig. 9.

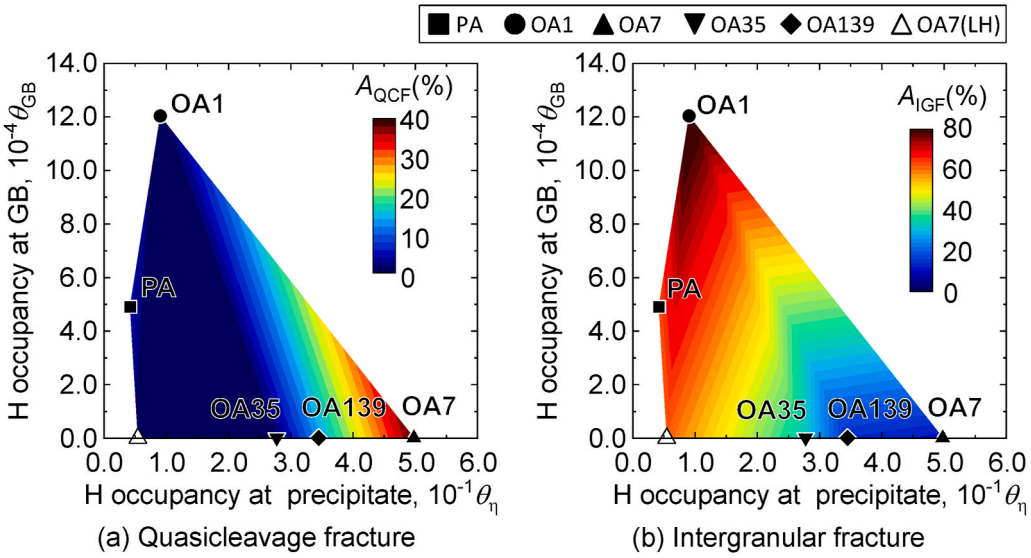

Fig. 11. Correlation between fracture morphology and hydrogen occupancy: Area fractions of (a) quasicleavage and (b) intergranular fracture modes mapped as functions of hydrogen occupancy at grain boundaries and precipitates. Data points represent specimens prepared by EDM: filled symbols denote high hydrogen content specimens processed in water, while open symbols indicate low hydrogen content specimens processed in oil.

alloys reveals several key insights: (i) this fracture mechanism is not confined to specific slip planes [48], (ii) quasicleavage facets present clear evidence of $MgZn_2$ precipitate debonding, and (iii) limited plastic deformation occurs in the cracking process. While we can identify the $MgZn_2$ interface as the crack origin, crack propagation involves complex mechanical factors. These factors include the orientation of the applied stress relative to the crack surface and slip planes. The intricate nature of these interactions makes definitive explanations challenging. Future research should focus on coupled simulation approaches that integrate hydrogen distribution and crystal plasticity. These advanced modeling techniques provide a comprehensive understanding of the mechanisms of quasicleavage cracking in Al–Zn–Mg alloys.

In this study, as shown in Fig. 12 (b), for OA139, when the hydrogen enrichment of semicoherent interfaces was weak, interface decohesion was relatively unlikely to occur. The aged microstructures of the Al–Zn–Mg alloys with limited semicoherent interfaces were prone to quasicleavage fracture. This kind of quasicleavage fracture originating from interface decohesion did not occur in steels or Ni-based alloys. In terms of the onset of semispontaneous debonding at the interface, it was determined that multiple strong hydrogen traps at the heterointerface, high hydrogen trapping energy at the matrix surface, and low surface energy were considered essential, as mentioned in the introduction [31]. The surface energies of aluminum, iron, and nickel were reported to be 0.82 J/m^2 for Al(111) [32], 2.358 for α-Fe(110) [33], and 1.92 for Ni (111) [81]. The high surface energies of these 3d transition metals indicated that semispontaneous interface decohesion did not occur in steels or Ni-based alloys. Reportedly, the vanadium carbide precipitate interface in ferritic steels was not separated by hydrogen trapping; in contrast, HE could be suppressed by preferentially trapping hydrogen at this interface [34,35]. Nagao et al. concluded that nanosized (Ti, Mo) C precipitates could trap hydrogen and improve HE in lath martensitic steels [82,83].

Finally, we propose a new strategy for preventing HE in Al–Zn–Mg alloys. There was a large difference in hydrogen solubility between the liquid and solid phases of aluminum, and the commercial alloy hydrogen content was considerably greater than the equilibrium hydrogen content. Reducing the hydrogen content in aluminum to suppress HE was not considered practical because it required a specific process, such as heat treatment in a vacuum. Therefore, it was preferable to use a technique that allowed for the presence of hydrogen in the alloy but made it practically harmless. Thus, it was advised to prepare sites where the hydrogen trapping energy was greater than that of the semicoherent interface (0.56 eV/atom) and insensitive to HE. Then, hydrogen was partitioned at these sites. Second-phase particles with high-energy internal hydrogen trapping sites could be considered for this application. In ferritic steels, internal hydrogen trapping in vanadium carbides was

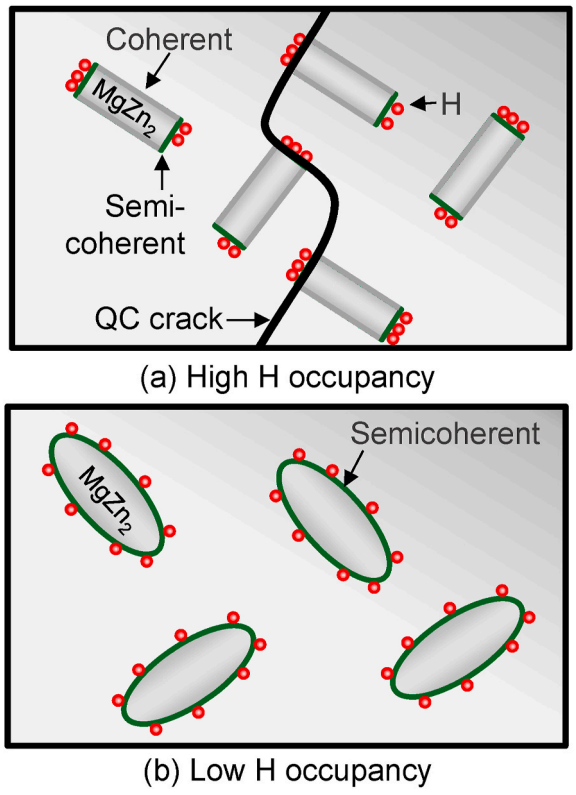

Fig. 12. Schematics of hydrogen trapping at the precipitate interface and the quasicleavage(QC) cracking mechanism. (a) limited semicoherent interface with high trapping energy and high hydrogen occupancy, causing hydrogen-induced interfacial decohesion. (b) precipitate with a semicoherent interface but low hydrogen occupancy, unlikely to serve as a fracture origin.

reported by Chen et al., who used atom probe tomography [84]. In aluminum, the internal hydrogen trapping energies of an Al_7Cu_2Fe particle were evaluated by first-principles calculations and were found to reach a maximum value of 0.56 eV/atom, which was equivalent to the trapping energies at semicoherent precipitate interfaces in $MgZn_2$ [85]. In our investigation, we discovered that the dispersion of particles with high internal hydrogen trapping energy, including Al_7Cu_2Fe, certain Mn-based particles, and the T phase ($Mg_{32}(Al, Zn)_{49}$), was advantageous for mitigating hydrogen embrittlement in Al–Zn–Mg(–Cu) alloys [86–88]. Leveraging these findings, we intend to adopt a novel alloy development approach for creating new aluminum alloys characterized by hydrogen embrittlement resistance and high strength, with the ultimate goal of practical utilization in the future.

5. Conclusions

The HE and associated hydrogen partitioning behaviors of Al–Zn–Mg alloys with different aged microstructures were investigated in this study. The following conclusions were obtained.

1. The area fraction of the HE fracture was dependent on the coherent interfaces of the aged precipitates. The conditions that resulted in the most intense intergranular and quasicleavage fracture modes were overaging for 1 h and 7 h, respectively.
2. The hydrogen trapping energy at the $MgZn_2$ semicoherent interface was determined to be 0.56 eV/atom by first-principles calculations. This energy was greater than that at the dislocations, vacancies, grain boundaries, and $MgZn_2$ coherent interfaces.
3. Quantitative analysis of hydrogen partitioning revealed that more than 90% of the hydrogen was concentrated at semicoherent interfaces of precipitates, and hydrogen occupancy at precipitate interfaces strongly correlated with the tendency for quasicleavage fracture. However, hydrogen occupancy at the grain boundaries and intergranular fracture were not correlated.
4. This study demonstrated that quasicleavage fracture originated from the decohesion of precipitate interfaces. Interface decohesion of coarse precipitates dispersed on grain boundaries, not the presence of hydrogen at the grain boundaries, induced intergranular fracture.

CRediT authorship contribution statement

Kazuyuki Shimizu: Writing – original draft, Visualization, Investigation, Formal analysis, Data curation, Conceptualization. **Hiroyuki Toda:** Writing – review & editing, Supervision, Funding acquisition, Conceptualization. **Kyosuke Hirayama:** Writing – review & editing, Investigation. **Hiro Fujihara:** Investigation. **Tomohito Tsuru:** Writing – review & editing, Visualization, Software, Formal analysis. **Masatake Yamaguchi:** Writing – review & editing, Visualization, Software, Formal analysis, Data curation. **Taisuke T. Sasaki:** Writing – review & editing, Formal analysis. **Masayuki Uesugi:** Writing – review & editing, Investigation. **Akihisa Takeuchi:** Writing – review & editing, Investigation.

Declaration of competing interest

The authors declare that they have no known competing financial interests or personal relationships that could have appeared to influence the work reported in this paper.

Acknowledgments

This work was supported by JST, CREST Grant Number JPMJCR1995, Japan. This study was partially supported by a Grant-in-Aid for Scientific Research from JSPS through Subject No. 23K04413, Japan, and by the NIMS Joint Research Hub Program. The financial support from the Light Metal Educational Foundation is gratefully acknowledged. The synchrotron experiments were performed at SPring-8 with the approval of the Japan Synchrotron Radiation Research Institute through proposal numbers 2020A1796, 2020A1531, 2020A1084, and 2022A1113.

Appendix A. Supplementary data

Supplementary data to this article can be found online at https://doi.org/10.1016/j.ijhydene.2025.02.123.

References

[1] Yamaguchi M, Ebihara KI, Itakura M, Kadoyoshi T, Suzudo T, Kaburaki H. First-principles study on the grain boundary embrittlement of metals by solute segregation: Part II. metal (Fe, Al, Cu)-hydrogen (H) systems. Metall. Mater. Trans. A Phys. Metall. Mater. Sci. 2011;42:330–9. https://doi.org/10.1007/s11661-010-0380-6. Springer US.
[2] Baba Y. Stress corrosion cracking of Al-Zu Mg alloys. J Jpn Inst Light Metals 1974; 24:227–38. https://doi.org/10.2464/jilm.24.227.
[3] Song RGG, Dietzel W, Zhang BJJ, Liu WJJ, Tseng MKK, Atrens A. Stress corrosion cracking and hydrogen embrittlement of an Al-Zn-Mg-Cu alloy. Acta Mater 2004; 52:4727–43. https://doi.org/10.1016/j.actamat.2004.06.023.
[4] Burleigh TD. The postulated mechanisms for stress corrosion cracking of aluminum alloys: a review of the literature 1980-1989. Corrosion 1991;47:89–98. https://doi.org/10.5006/1.3585235.
[5] Tsai TC, Chuang TH. Role of grain size on the stress corrosion cracking of 7475 aluminum alloys. Mater Sci Eng, A 1997;225:135–44. https://doi.org/10.1016/s0921-5093(96)10840-6.
[6] Li X, Zhang J, Cui Y, Djukic MB, Feng H, Wang Y. Review of the hydrogen embrittlement and interactions between hydrogen and microstructural interfaces in metallic alloys: grain boundary, twin boundary, and nano-precipitate. Int J Hydrogen Energy 2024;72:74–109. https://doi.org/10.1016/j.ijhydene.2024.05.257.
[7] Chen YS, Huang C, Liu PY, Yen HW, Niu R, Burr P, et al. Hydrogen trapping and embrittlement in metals – a review. Int J Hydrogen Energy 2024. https://doi.org/10.1016/j.ijhydene.2024.04.076.

[8] Sun H, Lv W, Yang Y, Li D, Yan L, Pang X, et al. Optimizing the hydrogen embrittlement resistance by tuning the structures of Cu-rich nanoprecipitates in high strength martensite stainless steels. Acta Mater 2023;246:118722. https://doi.org/10.1016/j.actamat.2023.118722.
[9] Gong P, Turk A, Nutter J, Yu F, Wynne B, Rivera-Diaz-del-Castillo P, et al. Hydrogen embrittlement mechanisms in advanced high strength steel. Acta Mater 2022;223:117488. https://doi.org/10.1016/j.actamat.2021.117488.
[10] Shibata A, Gutierrez-Urrutia I, Nakamura A, Okada K, Miyamoto G, Madi Y, et al. Three-dimensional propagation behavior of hydrogen-related intergranular cracks in high-strength martensitic steel. Int J Hydrogen Energy 2023;48:34565–74. https://doi.org/10.1016/j.ijhydene.2023.05.211.
[11] Ogawa Y, Noguchi K, Takakuwa O. Criteria for hydrogen-assisted crack initiation in Ni-based superalloy 718. Acta Mater 2022;229:117789. https://doi.org/10.1016/j.actamat.2022.117789.
[12] Khalid H, Shunmugasamy VC, DeMott RW, Hattar K, Mansoor B. Effect of grain size and precipitates on hydrogen embrittlement susceptibility of nickel alloy 718. Int J Hydrogen Energy 2024;55:474–90. https://doi.org/10.1016/j.ijhydene.2023.11.233.
[13] Takakuwa O, Ogawa Y, Miyata R. Antagonistic fatigue crack acceleration/deceleration phenomena in Ni-based superalloy 718 under hydrogen-supply. Sci Rep 2023;13:1–13. https://doi.org/10.1038/s41598-023-33761-4.
[14] Bhuiyan MSMSS, Toda H, Shimizu K, Su H, Uesugi K, Takeuchi A, et al. The role of hydrogen on the local fracture toughness properties of 7XXX aluminum alloys. Metall Mater Trans A Phys Metall Mater Sci 2018;49:5368–81. https://doi.org/10.1007/s11661-018-4880-0.
[15] Su H, Toda H, Shimizu K, Uesugi K, Takeuchi A, Watanabe Y. Assessment of hydrogen embrittlement via image-based techniques in Al–Zn–Mg–Cu aluminum alloys. Acta Mater 2019;176:96–108. https://doi.org/10.1016/j.actamat.2019.06.056.
[16] Wang Y, Liu J, Wang Z, Du F. Effect of pre-strain on hydrogen embrittlement of 7075 aluminum alloy and molecular dynamics simulation. Int J Hydrogen Energy 2024;88:626–37. https://doi.org/10.1016/j.ijhydene.2024.08.496.
[17] Wang M, Akiyama E, Tsuzaki K. Hydrogen degradation of a boron-bearing steel with 1050 and 1300MPa strength levels. Scr Mater 2005;52:403–8. https://doi.org/10.1016/j.scriptamat.2004.10.023.
[18] Bond GM, Robertson IM, Birnbaum HK. The influence of hydrogen on deformation and fracture processes in high-strength aluminum alloys. Acta Metall 1987;35:2289–96. https://doi.org/10.1016/0001-6160(87)90076-9.
[19] Iijima Y, Yoshida SI, Saitoh H, Tanaka H, Hirano KI. Hydrogen trapping and repelling in an Al-6 wt % Zn-2 wt % Mg alloy. J Mater Sci 1992;27:5735–8. https://doi.org/10.1007/BF01119730.
[20] Young GA, Scully JR. The diffusion and trapping of hydrogen in high purity aluminum. Acta Mater 1998;46:6337–49. https://doi.org/10.1016/S1359-6454(98)00333-4.
[21] Saitoh H, Iijima Y, Hirano K. Behaviour of hydrogen in pure aluminium, Al-4 mass % Cu and Al-1 mass% Mg2Si alloys studied by tritium electron microautoradiography. J Mater Sci 1994;29:5739–44. https://doi.org/10.1007/BF00349974.
[22] Smith SW, Scully JR. The identification of hydrogen trapping states in an Al-Li-Cu-Zr alloy using thermal desorption spectroscopy. Metall Mater Trans A Phys Metall Mater Sci 2000;31:179–93. https://doi.org/10.1007/s11661-000-0064-8.
[23] Nguyen D, Thompson AW, Bernstein IM. Microstructural effects on hydrogen embrittlement in a high purity 7075 aluminum alloy. Acta Metall 1987;35:2417–25. https://doi.org/10.1016/0001-6160(87)90139-8.
[24] Li Y, Wang Q, Zhang H, Zhu H, Wang M, Wang H. Role of solute atoms and vacancy in hydrogen embrittlement mechanism of aluminum: a first-principles study. Int J Hydrogen Energy 2023;48:4516–28. https://doi.org/10.1016/j.ijhydene.2022.10.257.
[25] Chen YS, Bagot PAJ, Moody MP, Haley D. Observing hydrogen in steel using cryogenic atom probe tomography: a simplified approach. Int J Hydrogen Energy 2019;44:32280–91. https://doi.org/10.1016/j.ijhydene.2019.09.232.
[26] Matsumoto R, Taketomi S. Molecular dynamics simulation of Surface-Adsorbed-Hydrogen-Induced Dislocation Motion in a thin film. Comput Mater Sci 2020;171:109240. https://doi.org/10.1016/j.commatsci.2019.109240.
[27] Chen BA, Liu G, Wang RH, Zhang JY, Jiang L, Song JJ, et al. Effect of interfacial solute segregation on ductile fracture of Al-Cu-Sc alloys. Acta Mater 2013;61:1676–90. https://doi.org/10.1016/j.actamat.2012.11.043.
[28] Li S, Li Y, Lo YC, Neeraj T, Srinivasan R, Ding X, et al. The interaction of dislocations and hydrogen-vacancy complexes and its importance for deformation-induced proto nano-voids formation in α-Fe. Int J Plast 2015;74:175–91. https://doi.org/10.1016/j.ijplas.2015.05.017.
[29] Khanzadeh M, Alipour H, Alahyarizadeh G. Understanding hydrogen behavior on aluminum: DFT investigations on adsorption and diffusion mechanisms. Int J Hydrogen Energy 2024;73:632–45. https://doi.org/10.1016/j.ijhydene.2024.06.068.
[30] Tsuru T, Yamaguchi M, Ebihara K, Itakura M, Shiihara Y, Matsuda K, et al. First-principles study of hydrogen segregation at the MgZn2 precipitate in Al-Mg-Zn alloys. Comput Mater Sci 2018;148:301–6. https://doi.org/10.1016/j.commatsci.2018.03.009.
[31] Tsuru T, Shimizu K, Yamaguchi M, Itakura M, Ebihara K, Bendo A, et al. Hydrogen-accelerated spontaneous microcracking in high-strength aluminium alloys. Sci Rep 2020;10:1–8. https://doi.org/10.1038/s41598-020-58834-6.
[32] Yamaguchi M, Ebihara KI, Itakura M, Tsuru T, Matsuda K, Toda H. First-principles calculation of multiple hydrogen segregation along aluminum grain boundaries. Comput Mater Sci 2019;156:368–75. https://doi.org/10.1016/j.commatsci.2018.10.015.
[33] Chamati H, Papanicolaou NI, Mishin Y, Papaconstantopoulos DA. Embedded-atom potential for Fe and its application to self-diffusion on Fe(1 0 0). Surf Sci 2006;600:1793–803. https://doi.org/10.1016/j.susc.2006.02.010.
[34] Takahashi J, Kawakami K, Kobayashi Y. Origin of hydrogen trapping site in vanadium carbide precipitation strengthening steel. Acta Mater 2018;153:193–204. https://doi.org/10.1016/j.actamat.2018.05.003.
[35] Takahashi J, Kawakami K, Tarui T. Direct observation of hydrogen-trapping sites in vanadium carbide precipitation steel by atom probe tomography. Scr Mater 2012;67:213–6. https://doi.org/10.1016/j.scriptamat.2012.04.022.
[36] Robertson IM, Sofronis P, Nagao A, Martin ML, Wang S, Gross DW, et al. Hydrogen embrittlement understood. Metall Mater Trans A Phys Metall Mater Sci 2015;46:2323–41. https://doi.org/10.1007/s11661-015-2836-1.
[37] Birnbaum HK, Sofronis P. Hydrogen-enhanced localized plasticity-a mechanism for hydrogen-related fracture. Mater Sci Eng, A 1994;176:191–202. https://doi.org/10.1016/0921-5093(94)90975-X.
[38] Robertson IM. The effect of hydrogen on dislocation dynamics. Eng Fract Mech 2001;68:671–92. https://doi.org/10.1016/S0013-7944(01)00011-X.
[39] Nagumo M. Hydrogen related failure of steels – a new aspect. Mater Sci Technol 2004;20:940–50. https://doi.org/10.1179/026708304225019687.
[40] Neeraj T, Srinivasan R, Li J. Hydrogen embrittlement of ferritic steels: observations on deformation microstructure, nanoscale dimples and failure by nanovoiding. Acta Mater 2012;60:5160–71. https://doi.org/10.1016/j.actamat.2012.06.014.
[41] Martin ML, Fenske JA, Liu GS, Sofronis P, Robertson IM. On the formation and nature of quasi-cleavage fracture surfaces in hydrogen embrittled steels. Acta Mater 2011;59:1601–6. https://doi.org/10.1016/j.actamat.2010.11.024.
[42] Deng Y, Barnoush A. Hydrogen embrittlement revealed via novel in situ fracture experiments using notched micro-cantilever specimens. Acta Mater 2018;142:236–47. https://doi.org/10.1016/j.actamat.2017.09.057.
[43] Shimizu K, Toda H, Kadogawa C, Fujihara H, Takeuchi A. Influence of nanovoids in the hydrogen embrittlement fracture of Al–Zn–Mg–Cu alloys. Materialia 2020;11:100667. https://doi.org/10.1016/j.mtla.2020.100667.
[44] Shibata A, Takahashi H, Tsuji N. Microstructural and crystallographic features of hydrogen- related crack propagation in low carbon martensitic steel. ISIJ Int 2012;52:208–12. https://doi.org/10.2355/isijinternational.52.208.
[45] Okada K, Shibata A, Takeda Y, Tsuji N. Crystallographic feature of hydrogen-related fracture in 2Mn-0.1C ferritic steel. Int J Hydrogen Energy 2018;43:11298–306. https://doi.org/10.1016/j.ijhydene.2018.05.011.
[46] Shibata A, Momotani Y, Murata T, Matsuoka T, Tsuboi M, Tsuji N. Microstructural and crystallographic features of hydrogen-related fracture in lath martensitic steels. Mater Sci Technol 2017;33:1524–32. https://doi.org/10.1080/02670836.2017.1312210.
[47] Zhang Z, Obasi G, Morana R, Preuss M. In-situ observation of hydrogen induced crack initiation in a nickel-based superalloy. Scr Mater 2017;140:40–4. https://doi.org/10.1016/j.scriptamat.2017.07.006.
[48] Hirayama K, Toda H, Suzuki T, Uesugi M, Takeuchi A, Ludwig W. Crystallographic analysis of hydrogen embrittlement behavior in aluminum alloy using diffraction contrast tomography. Mater Trans 2022;63:586–91. https://doi.org/10.2320/matertrans.MT-L2021020.
[49] Bhuiyan MS, Tada Y, Toda H, Hang S, Uesugi K, Takeuchi A, et al. Influences of hydrogen on deformation and fracture behaviors of high Zn 7XXX aluminum alloys. Int J Fract 2016;200:13–29. https://doi.org/10.1007/s10704-016-0092-z.
[50] Shimizu K, Toda H, Fujihara H, Hirayama K, Uesugi K, Takeuchi A. Hydrogen partitioning behavior and related hydrogen embrittlement in Al-Zn-Mg alloys. Eng Fract Mech 2019;216:106503. https://doi.org/10.1016/j.engfracmech.2019.106503.
[51] Toda H. 3D Image Reconstruction. X-Ray CT 2021:51–113. https://doi.org/10.1007/978-981-16-0590-1_3.
[52] Toda H, Shimizu K, Uesugi K, Suzuki Y, Kobayashi M. Application of dual-energy K-Edge subtraction imaging to assessment of heat treatments in Al-Cu alloys. Mater Trans 2010;51:2045–8. https://doi.org/10.2320/matertrans.L-M2010819.
[53] Shimizu K, Toda H, Uesugi K, Takeuchi A. Local deformation and fracture behavior of high-strength aluminum alloys under hydrogen influence. Metall Mater Trans A Phys Metall Mater Sci 2020;51:1–19. https://doi.org/10.1007/s11661-019-05304-y.
[54] Lorensen WE, Cline HE, Lorensen WE, Cline HE. Marching cubes: a high resolution 3D surface construction algorithm. Proc 14th Annu Conf Comput Graph Interact Tech SIGGRAPH 1987 1987;21:163–9. https://doi.org/10.1145/37401.37422.
[55] Kobayashi M, Toda H, Kawai Y, Ohgaki T, Uesugi K, Wilkinson DS, et al. High-density three-dimensional mapping of internal strain by tracking microstructural features. Acta Mater 2008;56:2167–81. https://doi.org/10.1016/j.actamat.2007.12.058.
[56] Vargas-Hernández RA. Bayesian optimization for calibrating and selecting hybrid-density functional models. J Phys Chem A 2020;124:4053–61. https://doi.org/10.1021/acs.jpca.0c01375.
[57] Monkhorst HJ, Pack JD. Special points for Brillouin-zone integrations. Phys Rev B 1976;13:5188. https://doi.org/10.1103/PhysRevB.13.5188.
[58] Methfessel M, Paxton AT. High-precision sampling for Brillouin-zone integration in metals. Phys Rev B 1989;40:3616. https://doi.org/10.1103/PhysRevB.40.3616.
[59] Bendo A, Matsuda K, Lervik A, Tsuru T, Nishimura K, Nunomura N, et al. An unreported precipitate orientation relationship in Al-Zn-Mg based alloys. Mater Char 2019;158:109958. https://doi.org/10.1016/j.matchar.2019.109958.
[60] Bendo A, Matsuda K, Lee S, Nishimura K, Nunomura N, Toda H, et al. Atomic scale HAADF-STEM study of η′ and η1phases in peak-aged Al–Zn–Mg alloys. J Mater Sci 2018;53:4598–611. https://doi.org/10.1007/s10853-017-1873-0.

[61] Koyama M, Ichii K, Tsuzaki K. Grain refinement effect on hydrogen embrittlement resistance of an equiatomic CoCrFeMnNi high-entropy alloy. Int J Hydrogen Energy 2019;44:17163–7. https://doi.org/10.1016/j.ijhydene.2019.04.280.
[62] Fan YH, Zhang B, Wang JQ, Han EH, Ke W. Effect of grain refinement on the hydrogen embrittlement of 304 austenitic stainless steel. J Mater Sci Technol 2019; 35:2213–9. https://doi.org/10.1016/j.jmst.2019.03.043.
[63] Bhadeshia HKDH, Bhadeshia HKDH, Bhadeshia HKDH. Prevention of hydrogen embrittlement in steels. ISIJ Int 2016;56:24–36. https://doi.org/10.2355/isijinternational.ISIJINT-2015-430.
[64] Ohte R, Yoshioka K, Uesugi T, Takigawa Y, Higashi K. Effects of Zr-addition on intergranular fracture of Al-Cu-Mg and Al-Zn-Mg-Cu alloys. J Jpn Inst Light Metals 2019;69:235–41. https://doi.org/10.2464/jilm.69.235.
[65] Razumovskiy VI, Ruban AV, Razumovskii IM, Lozovoi AY, Butrim VN, Vekilov YK. The effect of alloying elements on grain boundary and bulk cohesion in aluminum alloys: an ab initio study. Scr Mater 2011;65:926–9. https://doi.org/10.1016/j.scriptamat.2011.08.014.
[66] De Francisco U, Larrosa NO, Peel MJ. Hydrogen environmentally assisted cracking during static loading of AA7075 and AA7449. Mater Sci Eng, A 2020;772:138662. https://doi.org/10.1016/j.msea.2019.138662.
[67] Su H, Toda H, Masunaga R, Shimizu K, Gao H, Sasaki K, et al. Influence of hydrogen on strain localization and fracture behavior in Al–Zn–Mg–Cu aluminum alloys. Acta Mater 2018;159:332–43. https://doi.org/10.1016/j.actamat.2018.08.024.
[68] Militzer M, Sun WP, Jonas JJ. Modelling the effect of deformation-induced vacancies on segregation and precipitation. Acta Metall Mater 1994;42:133–41. https://doi.org/10.1016/0956-7151(94)90056-6.
[69] Enomoto T, Matsumoto R, Taketomi S, Miyazaki N. First-principles estimation of hydrogen occupancy around lattice defects in Al. Zair Soc Mater Sci Japan 2010; 59:596–603. https://doi.org/10.2472/jsms.59.596.
[70] Niordson CF, Gangloff RP, Martínez-pa E, Martínez-Pañeda E, Niordson CF, Gangloff RP. Strain gradient plasticity-based modeling of hydrogen environment assisted cracking. Acta Mater 2016;117:321–32. https://doi.org/10.1016/j.actamat.2016.07.022.
[71] Brinckmann S, Siegmund T, Huang Y. A dislocation density based strain gradient model. Int J Plast 2006;22:1784–97. https://doi.org/10.1016/j.ijplas.2006.01.005.
[72] Ismer L, Park MS, Janotti A, Van De Walle CG. Interactions between hydrogen impurities and vacancies in Mg and Al: a comparative analysis based on density functional theory. Phys Rev B Condens Matter 2009;80:1–10. https://doi.org/10.1103/PhysRevB.80.184110.
[73] Yamaguchi M, Itakura M, Tsuru T, Ebihara KI. Hydrogen-trapping energy in screw and edge dislocations in aluminum: first-principles calculations. Mater Trans 2021; 62:582–9. https://doi.org/10.2320/matertrans.MT-M2020375.
[74] Yamaguchi M, Tsuru T, Ebihara K, Itakura M. Surface energy reduction by dissociative hydrogen adsorption on inner surface of pore in aluminum. J Jpn Inst Light Metals 2018;68:588–95. https://doi.org/10.2464/jilm.68.588.
[75] Marioara CD, Lefebvre W, Andersen SJ, Friis J. Atomic structure of hardening precipitates in an Al-Mg-Zn-Cu alloy determined by HAADF-STEM and first-principles calculations: relation to η-MgZn2. J Mater Sci 2013;48:3638–51. https://doi.org/10.1007/s10853-013-7158-3.
[76] Steurer W, Dshemuchadse J. Crystal structures of intermetallic compounds. Intermetallics 2016:227–438. https://doi.org/10.1093/ACPROF:OSO/9780198714552.003.0007.
[77] Momma K, Izumi F. IUCr. VESTA 3 for three-dimensional visualization of crystal. volumetric and morphology data 2011;44:1272–6. https://doi.org/10.1107/S0021889811038970. Urn:Issn:0021-8898.
[78] Yamaguchi M, Ebihara KI, Tsuru T, Itakura M. First-principles calculations of hydrogen trapping energy on incoherent interfaces of aluminum alloys. Mater Trans 2023;64:2553–9. https://doi.org/10.2320/matertrans.mt-m2023106.
[79] Oriani RA. The diffusion and trapping of hydrogen in steel. Acta Metall 1970;18: 147–57. https://doi.org/10.1016/0001-6160(70)90078-7.
[80] Toda H, Oogo H, Horikawa K, Uesugi K, Takeuchi A, Suzuki Y, et al. The true origin of ductile fracture in aluminum alloys. Metall Mater Trans A Phys Metall Mater Sci 2014;45:765–76. https://doi.org/10.1007/s11661-013-2013-3.
[81] Tran R, Xu Z, Radhakrishnan B, Winston D, Sun W, Persson KA, et al. Surface energies of elemental crystals. Sci Data 2016 31 2016;(3):1–13. https://doi.org/10.1038/sdata.2016.80.
[82] Nagao A, Martin ML, Dadfarnia M, Sofronis P, Robertson IM. The effect of nanosized (Ti,Mo)C precipitates on hydrogen embrittlement of tempered lath martensitic steel. Acta Mater 2014;74:244–54. https://doi.org/10.1016/j.actamat.2014.04.051.
[83] Nagao A, Smith CD, Dadfarnia M, Sofronis P, Robertson IM. The role of hydrogen in hydrogen embrittlement fracture of lath martensitic steel. Acta Mater 2012;60: 5182–9. https://doi.org/10.1016/j.actamat.2012.06.040.
[84] Chen YS, Haley D, Gerstl SSAA, London AJ, Sweeney F, Wepf RA, et al. Direct observation of individual hydrogen atoms at trapping sites in a ferritic steel. Science 2017;355:1196–9. https://doi.org/10.1126/science.aal2418.
[85] Yamaguchi M, Tsuru T, Ebihara KI, Itakura M, Matsuda K, Shimizu K, et al. Hydrogen trapping in Mg2Si and Al7FeCu2 intermetallic compounds in aluminum alloy: first-Principles calculations. Mater Trans 2020;61:1907–11. https://doi.org/10.2320/matertrans.MT-M2020201.
[86] Shimizu K, Toda H, Fujihara H, Yamaguchi M, Uesugi M, Takeuchi A, et al. Hydrogen embrittlement and its prevention in 7XXX aluminum alloys with high Zn concentrations. Corrosion 2023;79:818–30. https://doi.org/10.5006/4300.
[87] Xu Y, Toda H, Shimizu K, Wang Y, Gault B, Li W, et al. Suppressed hydrogen embrittlement of high-strength Al alloys by Mn-rich intermetallic compound particles. Acta Mater 2022;236:118110. https://doi.org/10.1016/j.actamat.2022.118110.
[88] Wang Y, Sharma B, Xu Y, Shimizu K, Fujihara H, Hirayama K, et al. Switching nanoprecipitates to resist hydrogen embrittlement in high-strength aluminum alloys. Nat Commun 2022;13:1–8. https://doi.org/10.1038/s41467-022-34628-4.